

# Novel magnetic states and nematic spin chirality in the kagome lattice metal $\text{YMn}_6\text{Sn}_6$

Nirmal J. Ghimire,<sup>1,2,\*</sup> Rebecca L. Dally,<sup>3</sup> L. Poudel,<sup>3,4</sup> D. C. Jones,<sup>1,2</sup>  
D. Michel,<sup>1,2</sup> N. Thapa Magar,<sup>1</sup> M. Bleuel,<sup>3,4</sup> Michael A. McGuire,<sup>5</sup>  
J. S. Jiang,<sup>6</sup> J. F. Mitchell,<sup>6</sup> Jeffrey W. Lynn,<sup>3</sup> and I. I. Mazin<sup>1,2</sup>

<sup>1</sup>*Department of Physics and Astronomy,  
George Mason University, Fairfax, VA 22030*

<sup>2</sup>*Quantum Science and Engineering Center,  
George Mason University, Fairfax, VA 22030*

<sup>3</sup>*NIST Center for Neutron Research,  
National Institute of Standards and Technology, Gaithersburg, MD 20899*

<sup>4</sup>*Department of Materials Science and Engineering,  
University of Maryland, College Park, MD 20742*

<sup>5</sup>*Materials Science and Technology Division,  
Oak Ridge National Laboratory, Oak Ridge, Tennessee 37831, United States*

<sup>6</sup>*Materials Science Division, Argonne National Laboratory,  
9700 South Cass Avenue, Argonne, Illinois 60439, United States*

(Dated: July 7, 2020)

Identification, understanding, and manipulation of novel magnetic textures is essential for the discovery of new quantum materials for future spin-based electronic devices. In particular, materials that manifest a large response to external stimuli such as a magnetic field are subject to intense investigation. Here, we study the kagome-net magnet  $\text{YMn}_6\text{Sn}_6$  by magnetometry, transport, and neutron diffraction measurements combined with first principles calculations. We identify a number of nontrivial magnetic phases, explain their microscopic nature, and demonstrate that one of them hosts a large topological Hall effect (THE). We propose a new nematic chirality mechanism, reminiscent of the nematicity in Fe-based superconductors, which leads to the THE at elevated temperatures. This interesting physics comes from parametrically frustrated interplanar exchange interactions that trigger strong magnetic fluctuations. Our results pave a path to new chiral spin textures, promising for novel spintronics.

Kagome planes formed by Fe or Mn often have strong in-plane ferromagnetic (FM) exchange interactions which are not magnetically frustrated but still have features typical of kagome lattices - Dirac and flat bands - providing an ideal platform for novel topological states<sup>1-6</sup>. The interplanar interactions, on the other hand, are much weaker and often frustrated. FM ordering in the two-dimensional planes is then strongly suppressed due to the Mermin-Wagner theorem, enabling very strong magnetic fluctuations at elevated temperatures that provide fertile ground for new and interesting phenomena<sup>7-10</sup>.

$\text{YMn}_6\text{Sn}_6$  is a prototype for this materials class. It forms an hexagonal  $P6/mmm$  structure ( $a = 5.540 \text{ \AA}$  and  $c = 9.020 \text{ \AA}$ ) consisting of kagome planes  $[\text{Mn}_3\text{Sn}]$  separated by two inequivalent  $\text{Sn}_3$ , and  $\text{Sn}_2\text{Y}$  layers, *i.e.*,  $[\text{Mn}_3\text{Sn}][\text{Sn}_3][\text{Mn}_3\text{Sn}][\text{Sn}_2\text{Y}]$  [Figs. 1(a),(b)].  $\text{YMn}_6\text{Sn}_6$  is a good metal [Fig. 1(c)], and as such is expected to have relatively long-range exchange interactions, possibly including Ruderman-Kittel-Kasuya-Yosida (RKKY) coupling [Fig. 1(a)]. All Mn planes and in-plane nearest neighbor Mn-Mn bonds are crystallographically equivalent, but the interplanar Mn-Mn bonds along  $c$  are dramatically different, with a FM exchange interaction across the  $\text{Sn}_3$  layers, and antiferromagnetic (AF) across the  $\text{Sn}_2\text{Y}$  layers. These are frustrated by the *second* neighbor interaction across an intermediate  $\text{Mn}_3\text{Sn}$  layer ( $J_1$  and  $J_3$  are FM, while  $J_2$  is AF) and result in complex magnetic behaviors<sup>11,12</sup>. Below  $T_N \approx 345 \text{ K}$  [Fig. 1(d)], a commensurate collinear AF structure forms with the propagation vector

$\mathbf{k} = (0, 0, 0.5)$ . On cooling, an incommensurate phase quickly appears, which coexists with the commensurate phase in a narrow temperature range and becomes the only phase below 300 K<sup>11,13</sup>. Based on powder diffraction, the incommensurate state has been reported to have two (and even three at room temperature) nearly equal wave vectors,<sup>11</sup> which can be described as a staggered spiral, also dubbed the “double flat spiral,”<sup>14</sup> as depicted in Fig. 1(e). A magnetic field applied in the  $ab$ -plane induces multiple transitions seen in the magnetization and Hall resistivity<sup>12</sup>. Interestingly, an enigmatic topological Hall effect (THE) is observed at elevated temperatures, with the largest value around 245 K and a magnetic field of 4 T<sup>15</sup>. In this article, we determine the microscopic origin of the magnetic field-induced phases of  $\text{YMn}_6\text{Sn}_6$  and develop a theory describing the observed THE.

We first map out the different field-induced magnetic phases of  $\text{YMn}_6\text{Sn}_6$  with bulk measurements. Figure 2(a) shows the magnetization measurements of  $\text{YMn}_6\text{Sn}_6$  at two representative temperatures, 5 K and 245 K. For the magnetic field applied along the  $c$ -axis (red curve) the magnetization increases smoothly with field and for 5 K saturates slightly above 12 T, while the 245 K data show that the saturation field clearly decreases with increasing temperature. The effect of a magnetic field applied in the  $ab$ -plane ( $H_{ab}$ ) shown by the blue curves is more dramatic. At 5 K we see a sharp increase at 2 T indicative of a metamagnetic transition. A closer look reveals two close transitions, more apparent in the ac-susceptibility measurement [Fig. 2(b)]. Since the two transitions are very close, we denote the metamagnetic transition field by a single variable,  $H_1$ , for the remainder of the paper. As the field is further increased, the magnetization changes slope and increases continuously until  $H_2 = 7$  T. Above  $H_2$ , the magnetization grows slower, and saturates at  $H_3 = 9.8$  T. As temperature is increased,  $H_1$ ,  $H_2$  and  $H_3$  all shift to lower fields, and  $H_2$  and  $H_3$  become closer and merge. A phase diagram constructed from the ac-susceptibility is depicted in Fig. 2(b), with four main phases: (1)  $0 < H < H_1$ , (2)  $H_1 < H < H_2$ , (3)  $H_2 < H < H_3$  and (4)  $H > H_3$ . We call them distorted spiral (DS), transverse conical spiral (TCS), fan-like (FL), and forced-ferromagnetic (FF), respectively, based on the magnetic structures as detailed below. The narrow intermediate phases between FL and FF, and between TCS and FF are labelled “I” and “II”, respectively.

The Hall resistivity ( $\rho_H$ ) and magnetization ( $M$ ) as a function of  $H_{ab}$  at 5 K and 245 K are compared in Figs. 2(c) and (d), respectively. At 5 K,  $\rho_H$  has a very small negative slope in the DS phase. At  $H_1$ ,  $\rho_H$  shows a small jump but then decreases before increasing

rapidly to saturation in the FF state, forming a remarkable minimum in the FL phase. The behavior of  $\rho_H$  is significantly different at 245 K, where it exhibits a positive slope in the DS phase. At the metamagnetic transition ( $H_1$ ), it shows a sizable jump, then increases non-linearly with the magnetization in the TCS phase, which has been interpreted as the topological Hall effect (THE)<sup>15</sup>.

The zero-field neutron diffraction data are plotted in Fig. 3(a). A commensurate magnetic Bragg peak is observed at the onset of long range magnetic order, where  $\mathbf{k} = (0, 0, 0.5)$  and  $T_N = 345$  K, which quickly transforms into two distinct wave vectors. These two incommensurate structures coexist from their onset to the base temperature (12 K) determined by high resolution measurements [inset in Fig. 3(a)]. The two wave vectors  $(0, 0, k_{z,1})$  and  $(0, 0, k_{z,2})$  with  $k_{z,1} < k_{z,2}$  evolve smoothly with temperature along  $L$ , and  $|k_{z,1} - k_{z,2}|$  decreases with cooling. The two magnetic structures stemming from  $k_{z,1}$  and  $k_{z,2}$  are consistent with previous reports,<sup>11,14</sup> [see Fig. 1(e)] but with slightly different periodicities [Fig. S3(a)].

We now focus on the multiple magnetic phases induced via application of an external magnetic field in the  $ab$ -plane. Figures 3(b)-(c) show data taken about  $(0, 0, 2 - k_{z,n})$  ( $n = 1, 2$ ) for 100 K and 256 K, respectively. We find that  $k_{z,n}$  are almost field-independent, except for an abrupt shift to larger momentum for both magnetic peaks at  $H_1$ , which lies between 2.0 T and 2.5 T (between 1.5 T and 2.0 T for  $H_1$  at 256 K). Concomitant with these shifts are pronounced decreases in intensity of the Bragg peaks at  $(0, 0, L \pm k_{z,n})$  positions. The  $T = 100$  K data show a new commensurate structure emerging at  $H_2$  (6 T), with the wave vector  $(0, 0, k_c)$ , where  $k_c = 0.25$ , plus a satellite at  $2k_c$ -type positions which can be seen in Fig. 3(e) (discussed more below). These commensurate peaks coexist with the incommensurate peaks at 6 T and emerge at the cost of the incommensurate intensities [see Supplementary Information 1 (SI1) for details].

A 15 T magnet was employed to focus on the high field behavior, where a coarse instrumental resolution was used to compensate for the reduced intensities. The two incommensurate wave vectors are not resolvable with this resolution, but the data satisfactorily capture the overall high field behavior. Figure 3(f) shows that at 200 K the incommensurate peaks disappear above 7 T, similar to the observation that they are almost fully suppressed by 6 T in the 256 K high resolution data [Fig. 3(c)]. The  $\mathbf{k} = (0, 0, 0.25)$  commensurate structure at 100 K and 6 T in Fig. 3(b) can be seen at the same field in Fig. 3(e) at  $\mathbf{Q} = (0, 0, 2.25)$  with a satellite peak at  $\mathbf{Q} = (0, 0, 2.50)$ . Additionally, we see that all but the FF structures



disappear above 8 T as the spins become fully polarized. The high-field commensurate phase persists down to 10 K, shown in Fig. 3(d), but is shifted higher in field and is present between 6.5 T and 9.5 T.

The neutron data capture all the features observed in bulk magnetic measurements (Fig. 2). Below  $H_1$  there is very little change to the incommensurate peaks. At  $H_1$ , the wave vector positions change by  $\sim 3\%$  and intensity by up to 60% [see Fig. S3]. The  $H_1$  transition, which spans almost the entire temperature range of zero-field incommensurability, resembles a spin-flop transition, deduced from the magnetization data in Fig. 2(a). As discussed further in the theoretical section, this is a spin flop from a helical to cycloidal spiral. Comparison of the structure factor calculations for each magnetic structure to the data supports this assignment (see SI1 and Fig. S4 for details). At  $H_2$ , commensurate peaks with  $\mathbf{k} = (0, 0, 0.25)$ -type positions, and satellites at  $2k_c$ , emerge at the cost of the incommensurate structures. The commensurate peaks only appear in the FL phase. Curiously, however, a commensurate phase with propagation vector  $\mathbf{k} = (0, 0, 0.5)$  is seen to emerge at 300 K and low field (2 T) as seen in Fig. 3(g). This temperature and field reside within region ‘‘II’’ of the phase diagram in Fig. 2(b).

To understand the microscopic origin and nature of the different magnetic phases, we performed first principles Density Functional Theory (DFT) calculations and used the results to construct a mean field theory (MFT) at  $T=0$ . The details are presented in the methods and SI2, and here we summarize the main findings. First, DFT total energy calculations were performed and fit to the Hamiltonian (Eqn. 1)

$$\mathcal{H} = \sum_{i,j} J_n \mathbf{n}_i \cdot \mathbf{n}_j + \sum_{i,j} J_p \mathbf{n}_i \cdot \mathbf{n}_j + K \sum_i (n_i^z)^2 + \sum_i J^z n_i^z \cdot n_{i+1}^z + \sum_i \mathbf{n}_i \cdot \mathbf{H}, \quad (1)$$

where  $\mathbf{H}$  is the external field and  $\mathbf{n}$  is a unit vector along the local magnetization direction. The first sum runs over 6 nearest neighbors along the  $c$ -axis, the second over the first neighbors in the  $ab$ -plane, and the last three over all atoms ( $i+1$  denotes the nearest  $c$ -neighbor).  $K$  is the easy-plane single-ion anisotropy, and the Ising-type anisotropic exchange,  $J^z$ , is the only one allowed by symmetry for the vertical bonds. To account for Hubbard correlations, we added a DFT+U correction (see SI2). We found that the best description of the ground state is attained for  $U - J = 0.4 - 0.6$  eV, and in the following we use 0.4 (not unreasonable for a good metal). The results are shown in the Supplementary Table S1 for three models:

“full”, “reduced”, where  $J_{4-6}$  are absorbed into modified  $J_{2-3}$ , and “minimal”, where  $J_z$  is in addition combined with  $K$ . The “full” model has a staggered spiral as a ground state, as shown in Fig. 1(e), with the two angles  $\alpha = -22^\circ$  and  $\beta = 138^\circ$ , in reasonable agreement with the low temperature experimental  $\mathbf{k} \approx (0, 0, 0.25)$  described by the pitching angles  $-20^\circ$  and  $\beta = 110^\circ$  ( $\alpha + \beta = 90^\circ$ ). These angles were used in the “reduced” model,  $J_{2-3}$  calculations.

We now present the MFT results for the “minimal” and “reduced” models at  $T = 0$ . At  $H = 0$  one gets a staggered spiral<sup>14</sup>. Without  $K$ , the minimal model uniquely defines<sup>14</sup> the propagation vector  $k_z$  but is degenerate with respect to the plane in which the magnetic moments rotate. The anisotropy  $K$  locks the spins to the  $ab$ -plane. Results for the MFT are presented in Figs. 4(a)-(c) (see SI3 for details). The behavior for  $H||c$  is trivial: the helical spiral becomes longitudinal conical spiral (LCS) and gradually transforms into a field-polarized FM phase. For  $H||a$ , if there were no magnetic anisotropy ( $K = 0$ ), the staggered spiral would immediately flop from spins rotating in the  $ab$ -plane (helical) to those rotating in the  $bc$ -plane (cycloidal), which would then gradually cant into a transverse conical spiral (TCS) state, and eventually saturate. The magnetic anisotropy sets a finite spin-flop field  $H_1 \propto \sqrt{\langle J \rangle K}$ , where  $\langle J \rangle$  is the appropriately averaged  $J_{1-3}$  parameters. Below  $H_1$ , the spiral remains flat, but distorts slightly by canting each spin a little toward  $a$  (this is the DS phase). At  $H_1$ , the magnetization increases discontinuously. However, when the conical angle in the TCS phase above  $H_1$  becomes rather small, at the field  $H_2$  not that far from the saturation field, further canting gains too little energy and it becomes energetically favorable to flop back into the  $ab$ -plane, gaining back some of the anisotropy energy. The resulting phase, found by minimization of the minimal Hamiltonian, is a very unusual commensurate fan-like (FL) phase, depicted in Fig. 4(b). It can be described as a quadrupled structure along the  $c$ -axis, with spins deviating from the  $x$ -direction, the direction of the magnetic field, by the angles  $\gamma, \gamma, -\delta, \delta, -\gamma, -\gamma, \delta, -\delta$  which gradually decrease until the forced ferromagnetic (FF) state,  $\gamma = \delta = 0$ , is reached (see SI3 for details). The FL phase has a different periodicity for  $M_x$ , the projection of Mn moments onto the  $a$ -axis, and for  $M_y$ , the projection onto the perpendicular axis. The latter corresponds to  $k_c = 0.25$ , the former to  $k_c = 0.5$ , and the variation of amplitude of  $M_x$  is much smaller. The calculations [Fig. 4(c)] capture all features of the measured magnetization [Fig. 2(a)]. The predictions are also confirmed by our neutron data: the first spin-flop from a nearly-helical to a nearly-cycloidal spiral leads

to about 50% loss in the scattering intensity for  $(0, 0, L \pm k_{n,z})$ -type Bragg peaks (neutrons do not scatter off the  $M_z$  component in our geometry when the scattering vector is along  $L$ ), consistent with the discontinuous loss of intensity in the experiment (see SI1). In the minimal model the first spin-flop does not alter the periodicity; experimentally, however,  $k_z$  slightly increases in the TC phase. To understand this, we need to step back to the reduced model that retains separation of  $K$  and  $J^z$ . Then the MFT theory predicts a tiny shortening of the spiral pitch at  $H = H_1$ , on the scale of  $\approx 0.36J^z/J_1 \sim 1\%$  (see SI3). The FL phase also finds full confirmation in the experiment: at  $H = H_2$ , as predicted,  $k_z$  changes discontinuously to  $k_c = 0.25$  and the predicted weaker satellite at  $2k_c$  is observed as well.

We now focus on the topological Hall effect (THE) and show its origin in a fluctuation-driven nematic chirality. The THE appears in the TCS phase only. The fact that the THE is observed only at elevated temperatures while the TCS phase exists in the entire temperature range below 330 K, strongly suggests a key role of thermal fluctuations. It is worth remembering that the system is strongly 2D, with nearly two orders of magnitude difference between the  $ab$  and  $c$  couplings. In this case, by virtue of the Mermin-Wagner theorem, the mean field transition temperature of several thousand K is dramatically suppressed by large and relatively slow *in-plane* fluctuations. This is reminiscent of the famous nematic transition in the planar  $J_1 - J_2$  Heisenberg mode<sup>16</sup>, where these fluctuations can conspire in such a way to create a new, non-magnetic order parameter without a long-range magnetic order. This so-called nematic phase is realized in many Fe-based superconductors<sup>17</sup> and may be in other materials as well<sup>18</sup>.

We will argue now that similar physics may be realized in the TCS phase. The detailed theory is provided in SI4. Here we present a summary of the results. In a continuous approximation the TC spiral can be described as  $\mathbf{M} = \mathbf{M}_x + \mathbf{m}$ , where  $\mathbf{M}_x \parallel \hat{\mathbf{x}}$  is the induced magnetic moment and is a constant, and  $\mathbf{m} \perp \hat{\mathbf{x}}$  is a cycloidal spiral. It is also assumed that while the direction of the Mn moment can change and fluctuate, the amplitude stays the same. The topological chiral field given by the standard expression<sup>19</sup>  $b_x = \mathbf{M} \cdot (\partial_y \mathbf{M} \times \partial_z \mathbf{M}) = \partial_y \mathbf{M} \cdot (\partial_z \mathbf{M} \times \mathbf{M})$  is thus zero in the TCS phase (or in any phase) where  $\partial_y \mathbf{M} = \mathbf{0}$ , and hence there is no THE. However, addition of a magnon fluctuation, propagating along  $y$  with wave vector  $k_y$  gives  $\mathbf{M} = M_x \mathbf{x} + \mathbf{m} + \mu$  where the fluctuating moments rotate in a plane defined by a vector  $\omega$ , such that  $\omega \propto k_y$ . Then,  $\frac{\partial \mathbf{M}}{\partial z} = \frac{\partial \mathbf{m}}{\partial z} = \mathbf{m} \times \hat{\mathbf{x}}$ , and  $\frac{\partial \mathbf{M}}{\partial y} = \frac{\partial \mu}{\partial y} = \mu \times \omega$ . Using these equations on  $b_x$ , keeping only the

terms quadratic in  $\mu$ , and averaging over  $y$  gives  $b_x = -k_y m_z \mu^2$ , and, unless  $\omega \parallel \hat{\mathbf{x}}$ ,  $b_x \neq 0$ .

The physical meaning of this result is very simple; the TCS is one independent magnon short of a chiral combination of static magnons. Of all possible magnons there are some that generate positive chirality, but, by crystallographic symmetry, for each such magnon there is a partner with the same energy and opposite chirality. These two partners will be thermally excited with the same probability and will cancel each other, in the absence of an external field. However, they create non-zero chiral susceptibility, reminiscent of the nematic susceptibility in Fe-based superconductors. We find the chiral field in such a case to be:

$$\langle b_x \rangle = \text{const} \cdot T M_z^2 H_x = \text{const} \cdot (1 - M^2/M_s^2) T H_x. \quad (2)$$

The topological Hall resistivity ( $\rho^T$ ) is proportional to  $\langle b_x \rangle$ , and hence  $\rho^T$  can be calculated by Eqn. 2 using experimental parameters. It is to be noted that this expression is valid only for  $H_1 < H_x < H_2$  and the topological Hall resistivity is zero outside these limits. The theoretical  $\rho^T$  is plotted together with the measured data at  $T = 245$  K in Fig. 4(d). The inset shows the temperature dependence of  $\rho^T$  at a constant field of 4 T, which is linear in temperature as expected from Eqn. 2 ( $M_z$  depends on the temperature very weakly, as one can see from the experimental data in Fig. S15). The details of experimental and theoretical  $\rho^T$  are provided in the SI5. The remarkable agreement of the experimental data with this phenomenological model provides insight into the microscopic origin of the THE as stabilized by the thermal fluctuations creating an imbalance in the right and left handed transverse conical spirals - a nematic spin chirality. We want to point out that the exceptional agreement between theory and experimental THE, may be to some extent fortuitous, given the simplicity of the model and partitioning of the total  $\rho_H$  (discussed in detail in SI5), but provides a strong support to the presented physical picture, describing the observed THE in terms of nematic chirality.

In summary, we have identified two unique magnetic phases, TCS and FL, in  $\text{YMn}_6\text{Sn}_6$ , which emerge from the competitions between exchange interactions, the magnetic anisotropies, and Zeeman energy, with a remarkable agreement between bulk measurements, neutron diffraction, and first principles calculations. The THE in the TCS phase is of particular interest. As opposed to non-coplanar, and skyrmionic materials, this spiral magnet without static spin chirality forms a non-zero internal skyrmionic magnetic field dynamically, through preferential excitation of chiral fluctuations with a given handedness. This field

deflects the conducting charge and thus produces the extra component to the Hall effect, the THE. We call this effect “nematic chirality” by analogy with the nematic phase in Fe-based superconductors. Our results not only provide a new THE mechanism but also open promising avenues in looking for the chiral spin textures in new materials and at temperatures relevant for practical applications.

## METHODS

**Crystal growth and characterization.** Single crystals of  $\text{YMn}_6\text{Sn}_6$  were grown by the self-flux method. Y pieces (Alfa Aesar 99.9 %), Mn pieces (Alfa Aesar 99.95 %) and Sn shots (Alfa Aesar 99.999 %) were loaded in a 2 mL aluminum oxide crucible in a molar ratio of 1:1:20. The crucible was then sealed in a fused silica ampoule under vacuum. The sealed ampoule was heated to 1175 °C over 10 hours, homogenized at 1175 °C for 12 hours, and then cooled to 600 °C over 100 hours. Once the furnace reached 600 °C, the excess flux was decanted from the crystals using a centrifuge. Well-faceted hexagonal crystals as large as 100 mg were obtained. The crystal structure of the compound was verified by Rietveld refinement<sup>20</sup> of a powder x-ray diffraction pattern collected on pulverized single crystals at room temperature using a Rigaku Miniflex diffractometer. The Rietveld refinement was carried out using FULLPROF software<sup>21</sup>.

**Magnetic and transport property measurements.** dc susceptibility measurements were made using a Quantum Design VSM SQUID. dc magnetization and transport measurements were measured using a Physical Property Measurement System (PPMS). ac susceptibility measurements were carried out using a Quantum Design Dynacool PPMS. Resistivity and Hall measurements were performed following the conventional 4-probe method. Pt wires of 25  $\mu\text{m}$  diameter were attached to the sample with Epotek H20E silver epoxy. An electric current of 1 mA was used for the transport measurements. In magnetoresistance measurements, the contact misalignment was corrected by field symmetrizing the measured data.

**Neutron diffraction measurements.** A single-crystal was oriented in either the  $(H, 0, L)$  or  $(H, H, L)$  scattering plane on the triple-axis neutron spectrometer, BT-7<sup>22</sup> at the NIST Center for Neutron Research (NCNR). Elastic diffraction data were taken with  $E_i = E_f = 14.7$  meV and  $25' - 10' - 10' - 25'$  full- width-at-half-maximum (FWHM) collimators

were used before and after the sample, before the analyzer, and before the detector, respectively (unless otherwise noted). A superconducting 7 T vertical field magnet system with a top loading closed cycle refrigerator was used at the sample position such that the applied field was parallel to the  $[1, \bar{1}, 0]$  crystallographic direction. Bragg peaks were resolution limited and Gaussian in shape. Peaks were therefore fit to Gaussians with the FWHMs constrained to be that of the spectrometer resolution as determined by the program, ResLib<sup>23</sup>. Data using a superconducting 15 T vertical field magnet system were taken in the  $(H, H, L)$  scattering plane, where the magnetic field was also parallel to  $[1, \bar{1}, 0]$ . Moderately coarse resolution was used with  $-50' - 40'R - 120'$  collimators (where ‘R’ indicates radial) and a position sensitive detector. Throughout the manuscript, momentum is reported in reciprocal lattice units (r.l.u.) denoted by using  $H$ ,  $K$ , and  $L$ , where  $\mathbf{Q} [\text{\AA}^{-1}] = (\frac{4\pi}{\sqrt{3}a}H, \frac{4\pi}{\sqrt{3}a}K, \frac{2\pi}{c}L)$ .

**First principles calculations.** Most calculations were performed using the projected augmented wave pseudopotential code VASP<sup>24</sup>, and the gradient-dependent density functional of Ref. 25. For control purposes, some calculations were also repeated using the all-electron linearized augmented plane wave code WIEN2k<sup>26</sup>. Hubbard correlations were taken into account using the DFT+U with the fully-localized double counting prescription, and the spherically averaged correction  $U - J$ , with the value of  $U - J$  given in the text.

## REFERENCES

---

\* corresponding author; [nghimire@gmu.edu](mailto:nghimire@gmu.edu)

<sup>1</sup> Ghimire, N. J. & Mazin, I. I. Topology and correlations on the kagome lattice. *Nature Materials* **19**, 137–138 (2020).

<sup>2</sup> Kang, M. *et al.* Dirac fermions and flat bands in the ideal kagome metal FeSn. *Nature Materials* (2020). **19**, 163–169 (2020).

<sup>3</sup> Ye, L. *et al.* Massive Dirac fermions in a ferromagnetic kagome metal. *Nature* **555**, 638–642 (2018).

<sup>4</sup> Liu, E. *et al.* Giant anomalous Hall effect in a ferromagnetic kagome-lattice semimetal. *Nature Physics* **14**, 1125–1131 (2018).

- <sup>5</sup> Yin, J.-X. *et al.* Negative flat band magnetism in a spinorbit-coupled correlated kagome magnet. *Nature Physics* **15**, 443–448 (2019).
- <sup>6</sup> Zhang, Z.-Y. The quantum anomalous Hall effect in kagomé lattices. *Journal of Physics.: Condensed Matter* **23**, 365801 (2011).
- <sup>7</sup> Grohol, D. *et al.* Spin chirality on a two-dimensional frustrated lattice. *Nature Materials* **4**, 323–328 (2005).
- <sup>8</sup> Pereiro, M. *et al.* Topological excitations in a kagome magnet. *Nature Communications* **5**, 4815 (2014).
- <sup>9</sup> Hirschberger, M. *et al.* Skyrmion phase and competing magnetic orders on a breathing kagomé lattice. *Nature Communications* **10**, 5831 (2019).
- <sup>10</sup> Yin, J.-X. *et al.* Giant and anisotropic many-body spinorbit tunability in a strongly correlated kagome magnet. *Nature* **562**, 91–95 (2018).
- <sup>11</sup> Venturini, G., Fruchart, D. & Malaman, B. Incommensurate magnetic structures of  $\text{RMn}_6\text{Sn}_6$  ( $\text{R} = \text{Sc}, \text{Y}, \text{Lu}$ ) compounds from neutron diffraction study. *Journal of Alloys and Compounds* **236**, 102–110 (1996).
- <sup>12</sup> Uhlíová, K., de Boer, F. R., Sechovský, V. & Venturini, G. Magnetism of  $\text{YMn}_6\text{Sn}_6$  and  $\text{DyMn}_6\text{Ge}_6$  : Single-crystal Study. *WDS'06 Proceedings of Contributed Papers, Part III*, 48–53 (2006).
- <sup>13</sup> Zhang, H. *et al.* Topological magnon bands in a room-temperature kagome magnet. *Physical Review B* **101**, 100405(R) (2020).
- <sup>14</sup> Rosenfeld, E. V. & Mushnikov, N. V. Double-flat-spiral magnetic structures: Theory and application to the  $\text{RMn}_6\text{X}_6$  compounds. *Physica B* **403**, 1898–1906 (2008).
- <sup>15</sup> Wang, Q., Yin, Q., Fujitsu, S., Hosono, H. & Lei, H. Near-room-temperature giant topological Hall effect in antiferromagnetic kagome metal  $\text{YMn}_6\text{Sn}_6$ . *arXiv: 1906.07986*
- <sup>16</sup> Chandra, P., Coleman, P. & Larkin, A. I. Ising transition in frustrated Heisenberg models. *Physical Review Letters* **64**, 88–91 (1990).
- <sup>17</sup> Fernandes, R. M., Chubukov, A. V. & Schmalian, J. What drives nematic order in iron-based superconductors? *Nature Physics* **10**, 97–104 (2014).
- <sup>18</sup> Zhang, G., Glasbrenner, J. K., Flint, R., Mazin, I. I. & Fernandes, R. M. Double-stage nematic bond ordering above double stripe magnetism: Application to  $\text{BaTi}_2\text{Sb}_2\text{O}$ . *Physical Review B* **95**, 174402 (2017).

- <sup>19</sup> Nagaosa, N. & Tokura, Y. Topological properties and dynamics of magnetic skyrmions. *Nature Nanotechnology* **8**, 899–911 (2013).
- <sup>20</sup> McCusker, L. B., Von Dreele, R. B., Cox, D. E., Louër, D. & Scardi, P. Rietveld refinement guidelines. *J. Appl. Cryst.* **32**, 36–50 (1999).
- <sup>21</sup> Rodriguez-Carvajal, J. Recent advances in magnetic structure determination by neutron powder diffraction. *Physica B* **192**, 55–69 (1993).
- <sup>22</sup> Lynn, J. W. *et al.* Double-focusing thermal triple-axis spectrometer at the NCNR. *Journal of Research of the National Institute of Standards and Technology* **117**, 61–79 (2012).
- <sup>23</sup> Zheludev, A. ResLib ResolutionLibrary for MATLAB (version 3.4) (2009).
- <sup>24</sup> Kresse, G. & Furthmüller, J. Efficient iterative schemes for *ab initio* total-energy calculations using a plane-wave basis set. *Physical Review B* **54**, 11169–11186 (1996).
- <sup>25</sup> Perdew, J. P., Burke, K. & Ernzerhof, M. Generalized gradient approximation made simple. *Physical Review Letters* **77**, 3865–3868 (1996).
- <sup>26</sup> Blaha, P. & al., E. *An Augmented Plane Wave Plus Local Orbitals Program for Calculating Crystal Properties* (Vienna University of Technology, Austria, 2001).

## ACKNOWLEDGEMENTS

NJG acknowledges startup fund from George Mason University. Work in the Materials Science Division at Argonne National Laboratory (JFM and JSJ) was supported by the U.S. Department of Energy, Office of Science, Basic Energy Sciences, Materials Science and Engineering Division. Work at ORNL (MAM) was supported by the US Department of Energy, Office of Science, Basic Energy Sciences, Materials Sciences and Engineering Division. The identification of any commercial product or trade name does not imply endorsement or recommendation by the National Institute of Standards and Technology. The authors thank Predrag Nikolic and Christian Batista for insightful discussions.

## AUTHOR CONTRIBUTIONS

NJG conceived and coordinated the project. NJG and NTM grew the crystals. NJG, NTM, DM and DCJ characterized the samples. NJG and MAM performed the magnetic and magnetotransport measurements. JFM contributed to the magnetic and transport mea-



surements. JSJ contributed to the transport measurements. LP, RLD and JWL carried out neutron diffraction experiments. LP, MB, NJG and JWL performed SANS experiment. IIM carried out the first principles calculations and devised the phenomenological theory. NJG wrote the manuscript with contributions from RLD, JWL and IIM. All authors contributed to the discussion of the results.

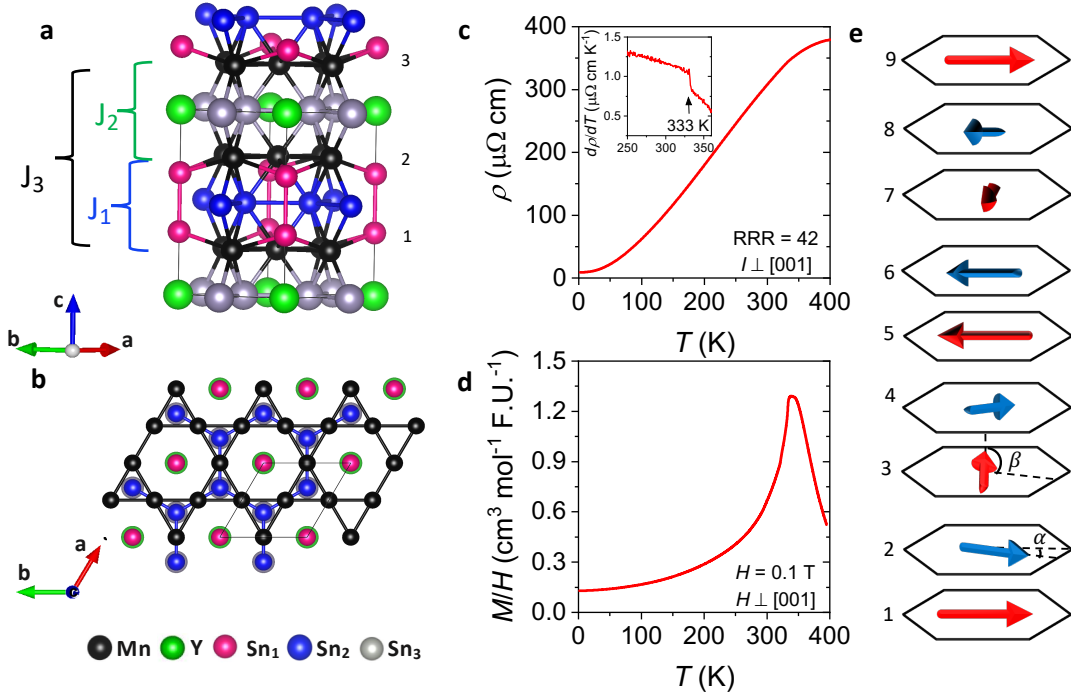


**FIG. 1 : Crystal structure, and electrical and magnetic properties of  $\text{YMn}_6\text{Sn}_6$ .** a) Sketch of the crystal structure of  $\text{YMn}_6\text{Sn}_6$ . b) Top view of the structure shown in panel (a). Within a unit cell shown by the dark solid lines, there are two kagome planes with the formula  $\text{Mn}_3\text{Sn}$  that are separated by  $\text{Sn}_3$  and  $\text{YSn}_2$  layers.  $J_i$ s are the exchange constants between different Mn layers. c) Electrical resistivity of  $\text{YMn}_6\text{Sn}_6$  as a function of temperature with the electric current applied in the  $ab$ -plane. Inset shows the temperature derivative of the electrical resistivity in the vicinity of  $T_N$ , which shows a jump at 333 K below which an incommensurate spiral state develops. The residual resistivity ratio ( $\text{RRR} = \rho_{400\text{K}}/\rho_{2\text{K}}$ ) is 42 indicating a good sample quality. d) Magnetic susceptibility ( $M/H$ ) of  $\text{YMn}_6\text{Sn}_6$  as a function of temperature. e) Incommensurate magnetic structure of  $\text{YMn}_6\text{Sn}_6$  in the absence of external magnetic field. Arrows represent the direction of ferromagnetic spins within a kagome plane. There is a small constant angle  $\alpha$  between the FM-coupled spins across the  $\text{Sn}_3$  layer, and  $\beta$  between the AF ones across the  $\text{Sn}_2\text{Y}$  which result in a spiral spin arrangement, where every other Mn layer forms a spiral with the pitch defined by  $\alpha + \beta \approx 90^\circ$  and the two spirals rotated by  $\alpha$  with respect to each other. The incommensurate spirals repeat after about four crystallographic unit cells or about nine Mn layers that are indicated by the numbers 1 through 9.

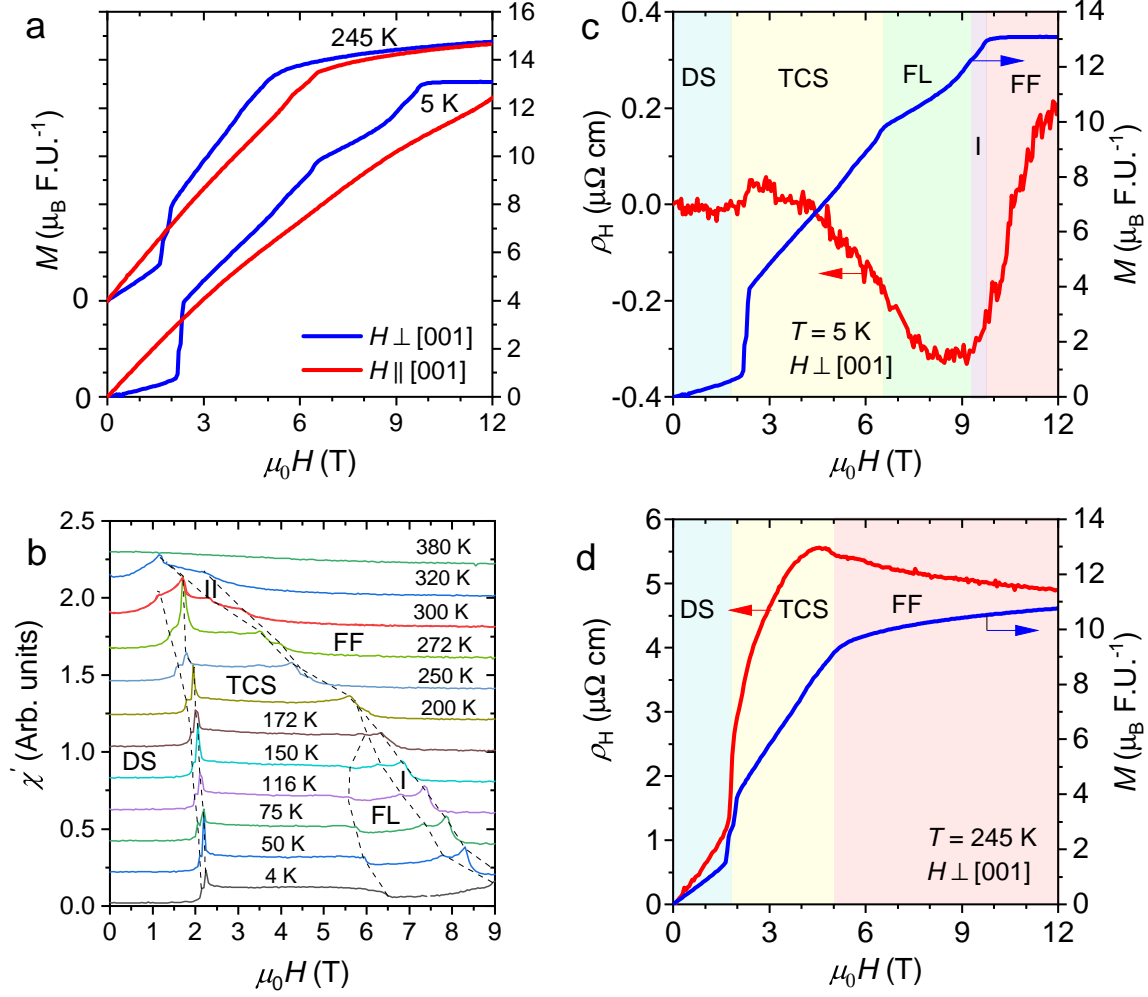


**FIG. 2 : Magnetization and Hall effect of  $\text{YMn}_6\text{Sn}_6$ .** a) Magnetization as a function of external magnetic field at 5 and 245 K with the magnetic field applied parallel and perpendicular to the  $c$ -axis. Data have been offset as indicated. b) Phase diagram of  $\text{YMn}_6\text{Sn}_6$  constructed from ac-susceptibility measurements. c) Hall resistivity (left axis) and magnetization (right axis) as a function of magnetic field applied in the  $ab$ -plane at 5 K, and d) at 245 K. DS, TCS, FL and FF stand for distorted spiral, transverse conical spiral, fan-like, and forced ferromagnetic phases, respectively.

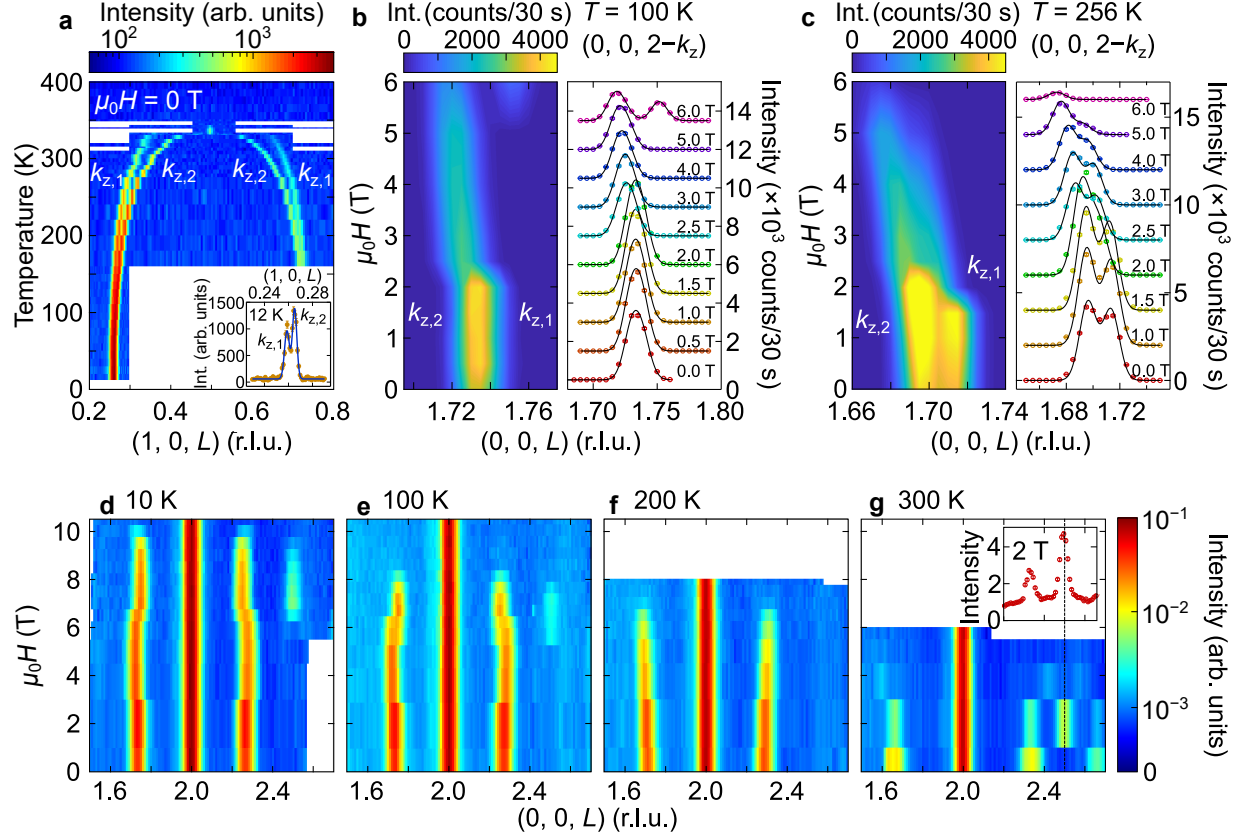


**FIG. 3 : Single crystal neutron diffraction of  $\text{YMn}_6\text{Sn}_6$ .** (a) Magnetic Bragg peaks tracked as a function of temperature. A commensurate magnetic peak at  $L = 0.5$  appears between 345 K and 330 K, and the two incommensurate magnetic structures stemming from the wave vectors  $k_{z,1}$  and  $k_{z,2}$  appear at 330 K and persist to the base temperature measured, 12 K. The inset, taken with high instrumental resolution, shows that the two wave vectors do not converge, even as they get closer with decreasing temperature. (b)-(c) Incommensurate magnetic Bragg peaks  $(0, 0, 2 - k_{z,n})$  ( $n = 1, 2$ ) tracked at 100 K and 256 K, respectively, as a function of applied magnetic field. The solid black lines in the right-hand panels of (b) and (c) are Gaussian fits to the data described in Methods. An offset was added between individual  $L$  scans for clarity. Offsets are 1500 counts/30 sec. for (b) and 2000 counts/30 sec. for (c). (d)-(g) Neutron diffraction data taken up to higher fields with a position sensitive detector and coarse resolution for (d) 10 K, (e) 100 K, (f) 200 K, and (g) 300 K. In these data,  $k_{z,1}$  and  $k_{z,2}$  are not resolvable, but the high fields at which the data were taken reveal the field ranges at which each of the magnetic phases are present. The inset of (g) is a cut taken from the main panel at 2 T, where the dashed black line shows that the new peak appearing at this field is commensurate at  $L = 2.5$ .

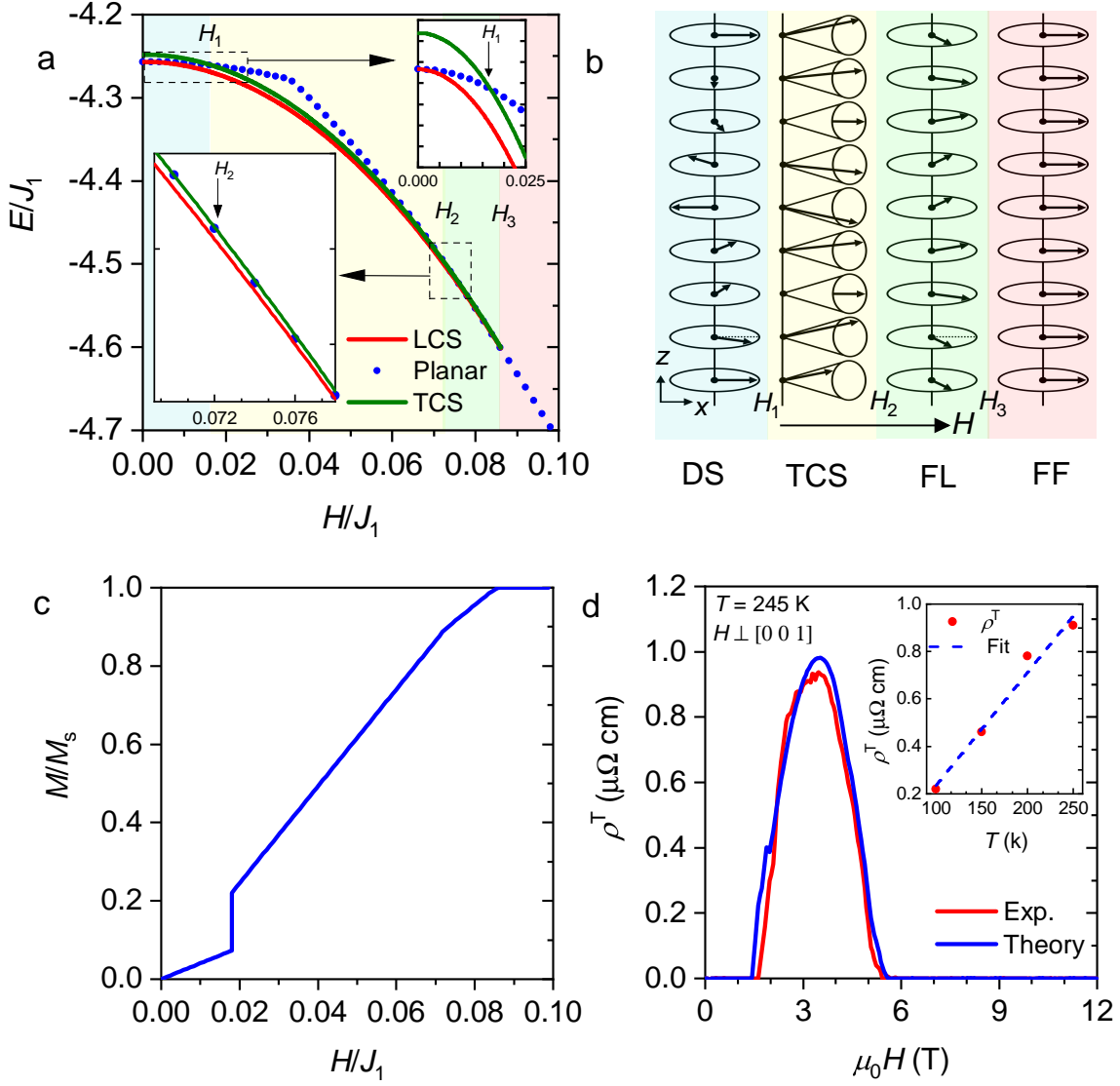


**FIG. 4 : First principles calculation and phenomenological model of nematic chirality for topological Hall effect.** a) Energy for different magnetic states as a function of reduced magnetic field obtained in MFT calculations. The planar state represented by the blue dotted line, has DS structure below the kink and FL structure above the kink. b) Sketch of different field-induced magnetic structures. DS, TCS, FL and FF stand for distorted spiral, transverse conical spiral, fan-like and forced ferromagnetic phases. c) Calculated magnetization as a function of in-plane field. d) Experimental and theoretical topological Hall resistivity as a function of external magnetic field at 245 K. Inset shows the temperature variation of the THE at 4 T below 250 K. The dashed line is a linear fit to the experimental data.

**Supplementary Information for:**  
**Novel magnetic states and nematic spin chirality in the kagome  
lattice metal  $\text{YMn}_6\text{Sn}_6$**

Nirmal J. Ghimire\*, Rebecca L. Dally, L. Poudel, D. C. Jones, D. Michel, N. Thapa  
Magar, M. Bleuel, Michael A. McGuire, J. S. Jiang, John F. Mitchell, Jeffrey W. Lynn,  
and I. I. Mazin

## SII. NEUTRON DIFFRACTION

One of the central motivations for investigating the properties of  $\text{YMn}_6\text{Sn}_6$  was to determine the origin of the observed topological Hall Effect (THE). One possibility was that a skyrmion lattice formed in the system, and therefore our first neutron experiments were using small angle neutron scattering (SANS) to search for skyrmions with the NG-7 SANS instrument at the NCNR using a 9 T horizontal field magnet ( $H \parallel [1, 1, 0]$ ) and exploring the temperature range from 4 K to 300 K. Figure S1(a) shows a background subtracted image over a wide wave vector range. No large scale magnetic structures were observed such as expected for a skyrmion lattice. Rather, just a single diffraction spot at a rather large (for SANS) wave vector was observed, indicating that long range magnetic order with an incommensurate modulation is realized. Fig. S1(b) shows an example of the field dependence of the magnetic order, demonstrating a complex series of magnetic phase transitions. Figure S1(c) shows cuts through the scattering at a field of 7 T for a series of temperatures, where it was first observed that there are two closely-spaced incommensurate wave vectors. To further elucidate the nature of the magnetic structures as a function of both magnetic field and temperature, wide angle diffraction data were collected as we now describe.

Figure S2 shows the variation of the incommensurate Bragg peaks at  $(1, 1, 0 - k_{z,n})$  with the external magnetic field applied in the  $ab$ -plane at 100 K and 256 K, similar to the data presented about  $(0, 0, 2 - k_{z,n})$  in Figs. 2(b) and (c). The momentum resolution in the measurement about the  $(1, 1, 0 - k_{z,n})$  peaks is much better than that about the  $(0, 0, 2 - k_{z,n})$  peaks, and as a result, the separation of  $k_{z,1}$  and  $k_{z,2}$  at 100 K is clearer in the former case. Determination of peak centering obtained from the fitting of  $(1, 1, 0 - k_{z,n})$  is thus unambiguous. We used the distance between the peak centers determined from the fitting of  $(1, 1, 0 - k_{z,n})$  to distinguish the behavior of the two peaks in  $(0, 0, 2 - k_{z,n})$  discussed in the main text. Additionally, the FWHM of the Gaussian fits were fixed to be that of the instrumental resolution as described in the Methods section. The integrated intensity obtained from the Gaussian fits are shown in Figs. S3(b) and (c). It can be seen from these figures that the percent decrease in intensity at the metamagnetic transition  $H_1$  is not as great as the  $(0, 0, 2 - k_{z,n})$  peaks, as expected for a helical to cycloidal transition. Intensities of the peaks measured at  $(1, 1, 0 - k_{z,n})$  are much weaker compared to the peaks measured at  $(0, 0, 2 - k_{z,n})$ , but it is still clear that at 6 T,  $k_{z,2}$  has practically no intensity

and the intensity of  $k_{z,1}$  is very weak. As the commensurate peaks emerge at 6 T [Figs. 3(b) and S3(a)], it suggests that they appear at the cost of the incommensurate peaks.

In Fig. S4, we plot the experimental ratio of intensity above versus below  $H_1$  together with the corresponding calculated ratios. This plot supports the first principles calculations results discussed in the main text of helical to cycloidal spin flop at  $H_1$ . Given a  $k_z$  and any  $\alpha$  value (the rotation angle between Mn layers separated by pure Sn layers), the calculated cycloidal:helical intensity ratio is 0.5 for  $(0, 0, L)$ -type peaks. This is because in the helical state, all spins lie perpendicular to  $(0, 0, L)$ -type scattering vectors, and neutrons are only sensitive to the component of a spin which is perpendicular to the scattering vector. When the moments flop into the  $(1, 1, 1)$  plane and the structure becomes cycloidal, half of the total spin magnitude is now projected along  $(0, 0, L)$ , thus reducing the intensity by half. There is generally much less of an intensity suppression after the transition for Bragg peaks at  $(H, H, L)$  positions where  $H$  is not equal to 0. This is because for a specific  $k_z$ , the cycloidal:helical structure factor ratios for a given peak do not change regardless of the value of  $\alpha$ . There are, however, slight differences in the ratios for different wave vectors, although they are small for the range of  $k_z$  observed in  $\text{YMn}_6\text{Sn}_6$ . The calculations used the different  $k_{z,n}$  values from the neutron data for the different temperatures and on either side of  $H_1$ . The  $(0, 0, L)$ -type peaks decrease in intensity more relative to the  $(H, H, L)$  ( $H \neq 0$ ) peaks across the  $H_1$  boundary, consistent with what would be observed for a helical to cycloidal spin-flop transition. Combined with the theoretical results, the neutron data do support the proposed helical to cycloidal spin-flop transition at  $H_1$ , especially when considering other complex incommensurate magnetic structures, such as the fan or spin density wave, which would bear the hallmark of Bragg peak harmonics and any harmonics are absent in the data presented here.

Additionally, we expect that immediately following the spin-flop transition, the cycloidal arrangement of spins would begin to cant along  $\mathbf{H}$ , forming a transverse conical structure. We confirmed this canting by tracking the net induced ferromagnetic component at the  $(0, 0, 4)$  Bragg peak as a function of applied magnetic field. In zero field, the intensity is purely nuclear in origin, with a field-induced intensity simply adding to the structural part. We see an abrupt emergence of an induced net ferromagnetic component at  $H_1$  for the 100 K and 256 K data, as shown in Figs. S5(a), and (b), respectively. We note that the 256 K data in Fig. S5(b) were taken with coarser instrumental resolution as can be discerned by



the  $x$ -axes in Figs. S5(a) and (b). The integrated intensity with respect to the zero-field intensity is shown for both temperatures in Fig. S5(c). The abrupt increase in intensity is indicative of a sudden canting of the moments towards the applied field direction,  $[1, \bar{1}, 0]$ , and the magnitude of this projection, in  $\mu_B^2 \text{Mn}^{-1}$ , is displayed on the right axis of Fig. S5(c). Note that the induced moment along the applied field direction is smaller at the higher temperature as expected, and both behaviors are completely consistent with bulk magnetization measurements presented in the main text [Fig. 2(a)].

## SI2. FIRST PRINCIPLES CALCULATIONS

Total energies of 10 different collinear ( $\alpha$  and  $\beta$  defined below are either 0 or  $180^\circ$ ) magnetic patterns were calculated in a supercell containing 8 Mn layers. Individual layers were ordered FM, and the selected patterns were: *u d d d d d d u*, *u d d d d d u d*, *u d d d d u d d*, *u d d d u u u d*, *u d d d u u u d*, *u d u d d u d u*, *u d u d u d d u*, *u d u d u d u d*, *u u d d u u d d*, *u u d u u u d d*, *u u u u u u u u*, where *u* stands for an up-polarized layer, and *d* for down-polarized. These were fitted to the following Hamiltonian:

$$2E = J_1 \cos \alpha + J_2 \cos \beta + 2J_3 \cos(\alpha + \beta) + J_4 \cos(2\alpha + \beta) + J_5 \cos(\alpha + 2\beta) + 2J_6 \cos(2\alpha + 2\beta) \quad (\text{S1})$$

where  $J_i$  are exchange interactions defined in Fig. S6,  $E$  is the energy per layer, and the angles  $\alpha$  and  $\beta$  define rotations between the planes bridged by  $\text{Sn}_3$  or  $\text{Sn}_2\text{Y}$  layers [see Fig. 1(a)]. At low temperature the wave vector is  $\approx \pi/2c$ . Fitting quality is very high, as shown in Fig. S7 (blue circles). The resulting values for  $J_{1-6}$  are  $-50.9$ ,  $9.1$ ,  $4.1$ ,  $-4.0$ ,  $-7.5$ , and  $-3.4$  meV. An immediate observation is that, indeed,  $J_1$  is strongly FM,  $J_2$  and  $J_3$  are both AF, but (i) their absolute values are quite far from the stability range of any spiral and (ii) longer-range interactions, especially  $J_5$ , are very important. A closer look reveals that the main factor preventing the formation of a spiral is the large  $J_1$ . Indeed, for a FM  $J_1$ , a spiral can only be stable if  $J_2/2(|J_1| + J_2) < J_3/J_1 < J_2/2(|J_1| - J_2)$ . This range, for  $J_2 \ll J_1$ , becomes infinitely narrow,  $J_2 - J_2^2/J_1 < 2J_3 < J_2 + J_2^2/J_1$ . Including the long-range interactions does not change this picture: the ground state is the collinear *uudd* pattern.

In many systems, the addition of Coulomb correlations reduces short-range magnetic couplings, but less so the long range ones. With this in mind, we repeated the calculations

by adding a Hubbard  $U$  in the common LDA+ $U$  approximation. Figure S7 (symbols other than blue circles) shows the fit quality, which is still high. Figure S8 shows how the fitted parameters vary as a function of the effective  $\tilde{U} = U - J$ .

It is instructive to look at the phase diagram in the “reduced” ( $J_1, J_2, J_3$  only) model. Figure S9 shows where our calculated effective exchange parameters fall at different  $\tilde{U} \approx 0.4$  eV and for  $\approx 0.6$  eV indeed a spiral is stable, and another for very large (likely unphysical for a good metal)  $U$ . It is also useful to compare the calculated magnetic moments on Mn with the experimental number of  $M_{\text{exp}} = 2.1$ . The fact that even at  $\tilde{U} = 0$  the moment is overestimated indicates a strongly fluctuating system and weak correlations.

On the other hand, an effective magnetic moment of  $\mu_{\text{eff}} = 3.6 \mu_B$  was extracted from the high-temperature susceptibility<sup>1</sup>, consistent with a spin  $S = 3/2$  (magnetic moment  $3 \mu_B$ ). Thus one can conclude that, despite the fact that for  $\tilde{U} \sim 2 - 3$  eV the system re-enters a spiral region, this part of the calculated phase diagram is unphysical. However, the range of  $0.4 - 0.6$  eV yields  $M \sim 2.7 \mu_B$  (Fig. S10) consistent with  $\mu_{\text{eff}}$ , and, after being reduced by fluctuations, with  $M_{\text{exp}}$ . As Fig. S11 illustrates, the calculated spiral angles at  $\tilde{U} = 0.4$  eV are  $\alpha = -22^\circ$  and  $\beta = 138^\circ$ . Aside from some overestimate in  $\beta$ , the overall agreement is good.

Plotting  $J_i$  as a function of distance clearly shows that it is inconsistent with the RKKY expression; in particular, it decays much more slowly than  $1/d^4$ . Nevertheless, there is no question that the interaction is transferred by conduction electrons. The conclusion is then that the Fermi surface must be rather complicated, and indeed it is. Another complication is that the standard RKKY formalism describes the interaction of localized moments in a nonmagnetic matrix. This is, obviously, inapplicable here. The closest analogy would be to start with a FM state and see whether it may be unstable against the formation of a spin density wave (SDW). To address this, we computed the Fermi surface, which is shown in Figs. S12(a) and (b).

Examining the Fermi surfaces, we see immediately that the spin-down surface is somewhat 2D and does not bear any obvious signature of nesting. The spin-up surface, on the other hand, is rather 3D, and has two pockets, one electron and one hole, which nest rather well with  $q_z(\text{\AA}^{-1}) = 0.235 \frac{2\pi}{c}$ , which agrees reasonably with the spiral vector in the experiment. This is illustrated in Fig. S12(c), showing a 2D cut of the pockets in question. Of course, this instability, which is similar in spirit, but rather different in details from RKKY, is

superimposed on top of other, short range interactions, which affect the final outcome.

### SI3. MEAN FIELD THEORY IN EXTERNAL MAGNETIC FIELD

Previous analyses were based on the assumption that only two ground states compete, a longitudinal conical spiral (LCS), where the field is oriented along the spiral vector, and the distorted spiral (DS)<sup>2</sup> where the field is applied normal to the spiral pitch. In the former, each moment is rotated out of the plane by the same amount to form a component parallel to the field. In the latter, the moments rotate in the plane, but retain the general spiral structure. We will show that this does not exhaust possible magnetic states.

Analyzing the complete model of Eq. S1 with an external field in an arbitrary direction is too cumbersome; for simplicity, we will reduce the model to the “standard”  $J_1 - J_2 - J_3$  one, keeping in mind that the physics of the spin-flop and spin-flip transitions is roughly the same. We then adjust the parameters to generate a SDW with  $q \approx (0, 0, 0.25)$ , and the pitching angles  $\alpha = -20^\circ$  and  $\beta = 110^\circ$  ( $\alpha + \beta = 90^\circ$ ), that is,  $J_2/J_1 = -0.364$ ,  $J_3/J_1 = 0.171$  (and,  $J_1 < 0$ ). For reference, the angles are in agreement with published analyses<sup>2</sup>,

$$\alpha = -\text{sign}(J_1 J_3) \cos^{-1} \left( \frac{J_2 J_3}{J_1^2} - \frac{J_3}{J_2} - \frac{J_2}{4J_3} \right), \quad (\text{S2})$$

$$\beta = \cos^{-1} \left( \frac{J_3 J_1}{J_2^2} - \frac{J_1}{4J_3} - \frac{J_3}{J_1} \right), \quad (\text{S3})$$

$$\alpha + \beta = \cos^{-1} \left( \frac{J_1 J_2}{8J_3^2} - \frac{J_2}{2J_1} - \frac{J_1}{2J_3} \right). \quad (\text{S4})$$

First, let us calculate the energy of the LCS state. Taking the same rotation angle  $\theta$  for all moments and assuming the ideal in-plane FM order, we can write the total energy per one  $1 \times 1 \times 4$  supercell as

$$E_{LCS} = 4(J_1 \cos \tau - J_2 \sin \tau) M_{\parallel}^2 + 4(J_1 + J_2 + 2J_3) M_{\perp}^2 - 8HM_{\perp} \quad (\text{S5})$$

where  $\tau = -\alpha = \beta - 90^\circ = 20^\circ$ ,  $M_{\parallel} = \cos \theta$ , and  $M_{\perp} = \sin \theta$  (as before, we normalize all interactions to unit moment). In the following we shall simplify notations by using  $e = E/|J_1|$ ,  $j_{2,3} = J_{2,3}/J_1$ , and  $h = H/|J_1|$ . The sign is kept in the second definition to harmonize notations with Refs. 2 and 3. Minimizing with respect to  $\theta$ , and using the selected parameters, we find

$$e_{LCS} = -4.257 - 46.443h^2. \quad (\text{S6})$$

The angle  $\theta$  changes gradually from  $\pi/2$  to 0, and saturates at  $h = 0.086$ . Next, we consider the field applied in the plane. Since the leading wave vector at low temperature, experimentally is close to  $(0, 0, 0.25)$ , and changes little with magnetic field (notwithstanding important, but small changes), we will consider a *commensurate* SDW in the  $1 \times 1 \times 4$  supercell, and, contrary to the previous works, we shall assign different angles  $\phi_i$  to each of the eight sites. In the absence of a field,  $\{\phi_2, \phi_3, \phi_4, \phi_5, \phi_6, \phi_7, \phi_8\} - \phi_1 = \{-\tau, \pi/2, \pi/2 - \tau, \pi, \pi - \tau, 3\pi/2, 3\pi/2 - \tau\}$ . The total energy now looks like ( $\phi_9 = \phi_1$ )

$$e_{DS} = - \sum_{j=1,4} \cos(\phi_{2j} - \phi_{2j-1}) - j_2 \sum_{j=1,4} \cos(\phi_{2j} - \phi_{2j+1}) - j_3 \sum_{i=1,8} \cos(\phi_i - \phi_{j+2}) - h \sum_{i=1,8} \cos(\phi_i). \quad (S7)$$

Minimizing this expression with respect to  $\phi_i$  reveals two interesting transition [Figs. 4(a) and (c)]. At  $h = h_f \approx 0.035$  the energy slope changes discontinuously, *i.e.*, the magnetization experiences a jump. At  $h = h_3 = 0.086$  (which represents  $H_3$  in the phase diagram), the moment saturates, and therefore  $\chi = dM/dH$  has a discontinuity. A closer inspection reveals that up to  $h_f$  the ground state is indeed a slightly distorted spiral (DS). Between  $h_f$  and  $h_3$ , however, it is a qualitatively different state, which we call fan-like (FL) phase, where the moments 1 and 2 are aligned ferromagnetically, and so are 5 and 6. They are gradually rotating with the field until they become parallel to the latter at  $h_3$ . At the same time, the pairs 3 and 4, and 7 and 8 are canted from the field in opposite directions. Thus, the moments form the following angles with the field:  $(\gamma, \gamma, -\delta, \delta, -\gamma, -\gamma, \delta, -\delta)$ . Immediately after the transition their values are  $\gamma = 77.25^\circ$  and  $\delta = -10.06^\circ$ . The normalized energy  $e = E/J_1$  as a function of the normalized field  $h = H/J_1$  of the LCS and planar (the planar state is DS below, and a FL structure above the kink at  $h_f$ ) phases are shown by the solid red line and dotted blue line, respectively in Fig. 4(a) of the main text.

However, without taking into account any anisotropy,  $E_{LCS}$  is always lower than either  $E_{DS}$  or  $E_{FL}$ , so the former would immediately flop and stay as such at all fields. So, let us include an easy-plane anisotropy, by adding a penalty term  $KM_\perp^2$ . The DS state is not affected. The spin-flopped LCS, competing with DS, is the transverse conical spiral (TCS), as described in the main text. Its energy is

$$E_{TCS} = 4(J_1 \cos \tau - J_2 \sin \tau)M_\parallel^2 + 4(J_1 + J_2 + 2J_3)M_\perp^2 - 8HM_\perp + 8KM_\perp^2. \quad (S8)$$

Since the average value of  $M_{\perp}^2$  in the TCS state is  $M^2/2$ , the penalty term for  $h = 0$  is  $8KM^2/2 = 4K^2$  (normalizing to  $M = 1$ ). This penalty will gradually decrease with  $h$ , as the canting toward the field direction increases. In short, it amounts to just adding a penalty term equal to  $const \times [1 - (h/h_{sat})^2]$  to Eq. S5. Energy of the TCS phase as a function of the magnetic field will then be different, which is shown in Fig. 4(a) as the green solid line.

At large fields, close to saturation, the energy gain derived from a larger spin susceptibility in the TCS phase is nearly lost, and at some critical field  $h_2 \approx 0.072$  ( $H_2$  in the phase diagram) it becomes energetically favorable to regain the anisotropy energy by flopping again into the  $ab$ -plane, into the FL phase (of course, the angles  $\gamma$  and  $\delta$  are now very small).

So the magnetic phases obtained are:

1) For the magnetic field along the  $c$ -axis: only the LCS phase is possible, and it gradually changes until the saturation is reached at  $h = h_3$ . 2) For the magnetic field in the  $ab$ -plane: At very small fields the state is  $DS$ . In this phase, magnetization increases with a rather small slope until the spin-flop field, proportional to  $\sqrt{K}$ , is reached ( $K = 0.01J_1$  was used in the plot, inspired by the calculated value of  $K \sim 0.2$  meV, and then  $h_{flop} = h_1 \approx 0.018$ ), at which point the state discontinuously transforms into the TCS phase *via* a spin flop. Highly unusual, it flops again at the field  $h_2$  into the FL phase (again, for our selection of  $K$ , it is  $\approx 0.072$ ), and finally saturates at  $h_3 = 0.086$ .

Let us now estimate the effect of the two spin-flops at,  $h_1$ , and  $h_2$ , on the spiral vector. In the above calculations we absorbed all magnetic anisotropies into one single-site term. However, there are no *a priori* arguments that anisotropic exchange (of the form  $J^z M_i^z M_j^z$ ) should be small compared to the single-site anisotropy. On the contrary, cases are known, when light magnetic  $3d$  ions are bridged by heavy nonmagnetic elements (as Sn and Y in our case) and the anisotropic exchange dominates, for instance in  $\text{CrI}_3$ , which, as well as  $\text{YMn}_6\text{Sn}_6$ , has a large magnetic moment.

Dividing the magnetic anisotropy into the single-site and exchange parts would not change the calculated phase diagram, except for one aspect. Indeed, while the onsite anisotropy does not change, in the lowest order, the spiral pitch, the anisotropic exchange does. Essentially, it adds an *antiferromagnetic* component to the ferromagnetic bonds and a *ferromagnetic* component to the antiferromagnetic bonds. Assuming that the leading contribution comes from the largest  $J$  (which is ferromagnetic  $J_1$ ), one can calculate the derivative  $d \cos(\alpha +$

$\beta)/dJ_1 = J_2/8J_3^2 + J_2/2J_1^2 - 1/2J_2 = J_1^{-1}(j_2/8j_3^2 + j_2/2j_1^2 - 1/2j_2 = -0.364J_1^{-1}$ . Adding an antiferromagnetic contribution to  $J_1$  (i.e.,  $\Delta J_1 > 0$ ) will have a negative effect  $\cos(\alpha + \beta)$ , that is to say,  $\alpha + \beta$  will be larger, and so will be the spiral  $q$ , in agreement with the experiment.

Calculations give  $K \approx -0.12$  meV/Mn (easy axis) and  $(J_1^z + J_2^z)/2 \approx 0.34$  meV (easy plane). This contribution is positive, i.e., antiferromagnetic. Assigning it entirely to  $J_1$ , we get  $J_1^z$  of the right sign, and  $J_1^z/J_1 \sim 0.34/51 \sim 0.7\%$ , in qualitative agreement with the experiment.

#### SI4. THEORY OF NEMATIC CHIRALITY IN $\text{YMn}_6\text{Sn}_6$

We now present a phenomenological theory of fluctuation-generated chirality and the topological Hall effect (THE) on a background of a static cycloidal or transverse conical magnetic spiral, which is observed at finite temperatures in an external magnetic field. We will assume that the amplitude of the Mn moments is constant (*i.e.*  $|\mathbf{M}| = 1$ ). The four phases of interest in  $\text{YMn}_6\text{Sn}_6$  are [see Figs. 2 and 4(a)]:

1. A longitudinal conical spiral (LCS) propagating along  $z$  in the field parallel to  $z$ , where the magnetic moment is described, in a continuous approximation, as

$$\mathbf{M} = \mathbf{M}_z + \mathbf{m} \quad (\text{S9})$$

$$\mathbf{M}_z = \text{const} \quad (\text{S10})$$

$$\frac{\partial \mathbf{m}}{\partial z} = m \times \mathbf{z}, \quad (\text{S11})$$

where  $\mathbf{M}_z \parallel \mathbf{z}$ , and  $\mathbf{m} \perp \mathbf{z}$ . Here and below  $\mathbf{z}$  is the unit vector.

2. A distorted spiral (DS) that appears in the in-plane field (parallel to  $x$ .) and below the first spin-flop (*i.e.*  $H_1$ ) transition. In the first approximation,

$$\mathbf{M} = \tilde{\mathbf{M}} + \mathbf{m} \quad (\text{S12})$$

$$\frac{\partial \tilde{\mathbf{M}}}{\partial z} = \tilde{\mathbf{M}} \times \mathbf{z} \quad (\text{S13})$$

$$\mathbf{m} = \tilde{M}_y \tilde{\mathbf{M}} \times \mathbf{z}, \quad (\text{S14})$$

where  $\tilde{\mathbf{M}} \perp \mathbf{z}$  and  $\mathbf{m} \perp \mathbf{z}$ .

3. A fan-like (FL) phase.

4. A transverse conical spiral (TCS) that appears in the in-plane field (parallel to  $x$  :)

$$\mathbf{M} = \mathbf{M}_x + \mathbf{m} \quad (\text{S15})$$

$$\mathbf{M}_x = \text{const} \quad (\text{S16})$$

$$\frac{\partial \mathbf{M}}{\partial z} = \frac{\partial \mathbf{m}}{\partial z} = \mathbf{m} \times \mathbf{x}, \quad (\text{S17})$$

where  $\mathbf{M}_x \parallel \mathbf{x}$ , and  $\mathbf{m} \perp \mathbf{x}$ .

We will now use the standard expression for the topological field, see *e.g.*, Eq. B4b in Ref. 4 (omitting the coefficient of 2):

$$b_\alpha = \varepsilon^{\alpha\beta\gamma} \mathbf{M} \cdot (\partial_\beta \mathbf{M} \times \partial_\gamma \mathbf{M}). \quad (\text{S18})$$

In the first case described above, that is, for an external field in the  $z$ -direction, the field couples with  $b_z$ , and

$$b_z = \mathbf{M} \cdot (\partial_x \mathbf{M} \times \partial_y \mathbf{M}). \quad (\text{S19})$$

In the ground state both  $\partial_x \mathbf{M}$  and  $\partial_y \mathbf{M} = 0$ , so generating a nonzero  $b_z$  requires exciting simultaneously two types of magnons, with two different in-plane vectors, which is an unlikely case.

In cases 2-4, *i.e.*, for an external field along  $x$ -direction, only  $b_x$  couples with the external field, so without losing generality we can rewrite it as:

$$b_x = \mathbf{M} \cdot (\partial_y \mathbf{M} \times \partial_z \mathbf{M}) = \partial_y \mathbf{M} \cdot (\partial_z \mathbf{M} \times \mathbf{M}). \quad (\text{S20})$$

In the ground state  $\mathbf{M}$  only varies with  $z$ , so this expression is obviously zero. In a planar-helical ( $\mathbf{H} = \mathbf{0}$ ) state  $\partial_z \mathbf{M} \times \mathbf{M}$  is parallel to  $z$ , and averages to zero over all planes. So, let us concentrate on the state (4). Let us then write  $\mathbf{M}$  as

$$\mathbf{M} = M_x \mathbf{x} + \mathbf{m} + \mu \quad (\text{S21})$$

where, as mentioned,  $\mathbf{m} \perp \mathbf{x}$ , and  $\mu$  represents a magnon propagating along  $y$  (in order to have nonzero  $\partial_y \mathbf{M}$ ) in a plane defined by a vector  $\omega$ , such that  $\omega \propto k_y$ . Then

$$\frac{\partial \mathbf{M}}{\partial z} = \frac{\partial \mathbf{m}}{\partial z} = \mathbf{m} \times \mathbf{x} \quad (\text{S22})$$

$$\frac{\partial \mathbf{M}}{\partial y} = \frac{\partial \mu}{\partial y} = \mu \times \omega \quad (\text{S23})$$

Let us now calculate  $b_x$

$$b_x = (M_x \mathbf{x} + \mathbf{m} + \boldsymbol{\mu}) \cdot ((\boldsymbol{\mu} \times \boldsymbol{\omega}) \times (\mathbf{m} \times \mathbf{x})) \quad (\text{S24})$$

$$= \boldsymbol{\mu} \cdot ((\boldsymbol{\mu} \times \boldsymbol{\omega}) \cdot \mathbf{x}) \mathbf{m} - [(\boldsymbol{\mu} \times \boldsymbol{\omega}) \cdot \mathbf{m}] \mathbf{x} \quad (\text{S25})$$

where the terms linear in  $\boldsymbol{\mu}$  are dropped because they average to zero upon integrating over  $y$ . Continuing with the expansion,

$$b_x = (\boldsymbol{\mu} \cdot \mathbf{m})[\boldsymbol{\mu} \cdot (\boldsymbol{\omega} \times \mathbf{x})] - (\boldsymbol{\mu} \cdot \mathbf{x})[\boldsymbol{\mu} \cdot (\boldsymbol{\omega} \times \mathbf{m})] \quad (\text{S26})$$

It is important to note that we can consider each  $ab$  plane independently, as they are capable of fluctuating independently. Let us for simplicity consider the case  $\boldsymbol{\omega} \parallel \mathbf{z}$ . Then

$$b_x = (\boldsymbol{\mu} \cdot \mathbf{m})[\boldsymbol{\mu} \cdot \mathbf{y}] - (\boldsymbol{\mu} \cdot \mathbf{x})[\boldsymbol{\mu} \cdot (\boldsymbol{\omega} \times \mathbf{m})] = k_y m_z \mu^2 \quad (\text{S27})$$

Now for  $\boldsymbol{\omega} \parallel \mathbf{y}$ , after averaging over  $y$ , we get

$$b_x = -k_y m_z \mu^2 \quad (\text{S28})$$

and, if  $\boldsymbol{\omega} \parallel \mathbf{x}$ ,  $b_x = 0$ . We saw that there are some magnons in the system that propagate along  $y$  and can generate a topological magnetic field  $b_x$ , which couples to the external field  $H_x$ . By definition, the energy cost to excite such a magnon is  $Ak_y^2 JM^2$ , where  $J$  is the ferromagnetic exchange coupling in the plane. As we have seen,  $b_x = Bk_y$  for magnons with some polarization planes and  $-Bk_y m_z$  for others. The coupling term must be  $CH_x k_y$ . The constants  $B$  and  $C$  are proportional to  $m_z$ , and are different for each plane. Let us calculate the expectation value for the  $\langle b_x \rangle$  for one plane and one type of magnons:

$$\langle b_x \rangle = \frac{\int Bk_y e^{-Ak_y^2 J/T} (e^{CH_x k_y/T} - e^{-CH_x k_y/T}) dk_y}{\int e^{-Ak_y^2 J/T} (e^{CH_x k_y/T} + e^{-CH_x k_y/T}) dk_y} \quad (\text{S29})$$

$$= \frac{\int Bk_y e^{-Ak_y^2 J/T} \sinh(CH_x k_y/T) dk_y}{\int e^{-Ak_y^2 J/T} \cosh(CH_x k_y/T) dk_y} \quad (\text{S30})$$

$$\approx \frac{\int Bk_y e^{-Ak_y^2 J/T} (CH_x k_y/T) dk_y}{\int e^{-Ak_y^2 J/T} dk_y}. \quad (\text{S31})$$

In the last line we made use of the fact that  $J \gg T$ . From that,

$$\langle b_x \rangle = BCH_x T/AJ = \text{const} \cdot TM_z^2 H_x = \text{const} \cdot (1 - M^2/M_s^2)TH_x, \quad (\text{S32})$$

where  $M_s$  is the saturated magnetization.



A requirement for this scenario is a conical spiral rotating in a plane perpendicular to the external field. It is also essential that the coupling between the planes is weak, allowing magnons to be excited independently in each plane. It is also obvious from the general theory of the THE that conduction electrons should be strongly coupled to the magnetic moments. This implies that, as in MnSi<sup>4</sup>, they belong to the same system and have strong Hund's rule coupling. This is fulfilled here because both the moments and the conductivity are due to Mn *d*-electrons, but may not work well for, say, rare earth based spiral magnets. In any event, the scale of the effect must be very material-dependent (coefficients *B* and *C* above), and its microscopic evaluation may be challenging.

## SI5. TOPOLOGICAL HALL EFFECT

The Hall effect, in general, is an intrinsic property of a conductor due to the Lorentz force experienced by the charge carriers. In systems with spontaneously broken time-reversal symmetry, an additional contribution, independent of the Lorentz force, is observed which is proportional to the magnetization *M* and is called the anomalous Hall effect (AHE)<sup>5</sup>. In materials with spin textures allowing a non-zero scalar spin chirality defined by  $\mathbf{S}_i \cdot (\mathbf{S}_j \times \mathbf{S}_k)$ , where *i, j, k* are neighboring spins (equivalent, in the continuous approximation, to Eq. S18), an additional component of the Hall effect is permitted due to the real-space Berry phase called the topological Hall effect (THE)<sup>6,7</sup>. Thus, a Hall resistivity can be expressed as:

$$\rho_H = \rho^O + \rho^A + \rho^T. \quad (\text{S33})$$

Here  $\rho^O = R_0 B$  is the ordinary Hall resistivity, where *R*<sub>0</sub> is the coefficient defined by the number of carriers (weighted with their mobility, for a multiband metal),  $B = \mu_0 H$ , and *H* is the external magnetic field.  $\rho^A = R_s \mu_0 M$  is the conventional anomalous Hall resistivity where *R*<sub>s</sub> is the coefficient of the conventional AHE.  $\rho^T$  is the Hall resistivity contribution from the THE. *R*<sub>s</sub> and *R*<sub>0</sub> can be estimated from the high magnetic field component of the magnetization and the Hall resistivity (in the forced ferromagnetic state where the magnetization saturates), where  $\rho^T = 0$ . Thus, Eqn. S33 takes the form:

$$\rho_H = R_0 B + \mu_0 R_s M. \quad (\text{S34})$$

The intercept of  $\rho_H/M$  vs  $B/M$  gives  $\mu_0 R_s$  while the slope gives  $R_0$ . The  $R_0$  estimated this way is correct in the forced ferromagnetic (FF) state. However, we cannot assume the same in the low field region where the Fermi surface (and hence the carrier concentration) is different from that in the FF state. To address this discrepancy, we use the following principle to estimate the normal component of the Hall resistivity that needs to be subtracted (together with the anomalous Hall resistivity) from the measured Hall resistivity to get the topological contribution. Despite  $M$  (and thus  $\rho^A$ ) changing at  $H_1$  nearly discontinuously, up to a small spin-orbit coupling there is no discontinuity in the number of carriers. At  $H_2$ , in principle, there might be a discontinuous change in  $R_0$ , but since both TCS and FL phases at this point only slightly deviate from the FF state, this change must be small. Thus, to a good accuracy, we can assume that  $R_0$  changes smoothly between the low-field regime ( $H < H_1$ ), where we can estimate it from the difference between  $\rho_H$  and  $\rho^A$ , and the high-field regime, where it is the only component changing. We estimated the smooth change of the normal component of the Hall resistivity by interpolating a cubic spline between  $H_1$  and  $H_2$  in the  $\rho_H - \rho^A$  data. The measured  $\rho_H$  and its different components are shown in Fig. S13(a). Together with  $\rho^O$  estimated as explained above (green solid line labelled 1), we also show, for comparison,  $\rho^O$  obtained by using a simple linear interpolation between  $H_1$  and  $H_2$  in the  $\rho_H - \rho^A$  data (orange dashed line labelled 2), and  $\rho^O$  calculated using  $\rho^O = R_0 B$ , where  $R_0$  is obtained in the FF state (brown dashed line labelled 3). The THE obtained using #1 and #3  $\rho^O$  are depicted in Figs. S13(c) and (d), respectively. The amplitude of the THE obtained by using #3  $\rho^O$  is slightly larger than that using #1  $\rho^O$ , which is essentially due to an improper subtraction of the normal Hall component in the former case as can be seen in Fig. S13(d), where using #3  $\rho^O$  still gives some THE contribution below  $H_1$ , where it is not expected. The amplitude of the THE obtained using #2  $\rho^O$  lies between that obtained with the other two  $\rho^O$  (not shown).

In Fig. S13(b), we show the calculated THE using Eqn. S32 from the theoretical model. As the THE is proportional to  $\langle b_x \rangle$ , in the calculation we used:

$$\rho^T = \kappa(1 - M^2/M_s^2)TH \quad (\text{S35})$$

where  $M$  is the magnetization measured in the magnetic field  $H$ ,  $M_s$  is the saturated magnetization,  $T$  is temperature, and  $k$  is the proportionality constant. In the calculation, the experimental magnetization data measured at  $T = 245$  K are used (black solid line). It is to

be noted that Eqn. S35 is valid only in the TCS phase i.e. between  $H_1$  and  $H_2$ . Therefore, after calculating  $\rho^T$  in the entire field range, we determined the  $\rho^T$  obtained outside the TCS phase as a background by interpolating a straight line between  $H_1$  and  $H_2$  (dashed pink line) and subtracted the background to obtain the THE in the TCS phase (solid blue line). This theoretical  $\rho^T$  is compared to the experimental data in Fig. S13(c), which is also shown in Fig. 4(d). In Fig. S13(d), we compare the theoretical THE with the experimental THE obtained by using #3  $\rho^O$  discussed above. From Figs. S13(c) and (d), we see that the theoretical model describes the experimental data fairly well irrespective of the method used to estimate the normal Hall component (which is much smaller than the THE). The only difference in the calculated THE in these two cases is the proportionality constant  $\kappa$ .

To provide further evidence of the THE in  $\text{YMn}_6\text{Sn}_6$  for the in-plane magnetic field, we show the Hall resistivity measured with the magnetic field in the  $ab$ -plane and along the  $c$ -axis in Fig. S14(a). This shows that a topological Hall contribution appears between around 2 T and 5 T only in the case when the magnetic field is applied in the  $ab$ -plane. The corresponding magnetization data for comparison are presented in Fig. 2(a). The Hall resistivity measured with magnetic field applied in the  $ab$ -plane at 5 K and 245 K is presented in Fig. S14(b) and the corresponding magnetization data are presented in Fig. S14(c). The difference in magnetization between 5 K and 245 K below 6 T is small, but the Hall resistivity at 245 K is highly enhanced as compared to that at 5 K, which also supports the presence of a topological contribution to the Hall resistivity at 245 K.

## SI6. SUPPLEMENTARY REFERENCES

---

\* corresponding author; [nghimire@gmu.edu](mailto:nghimire@gmu.edu)

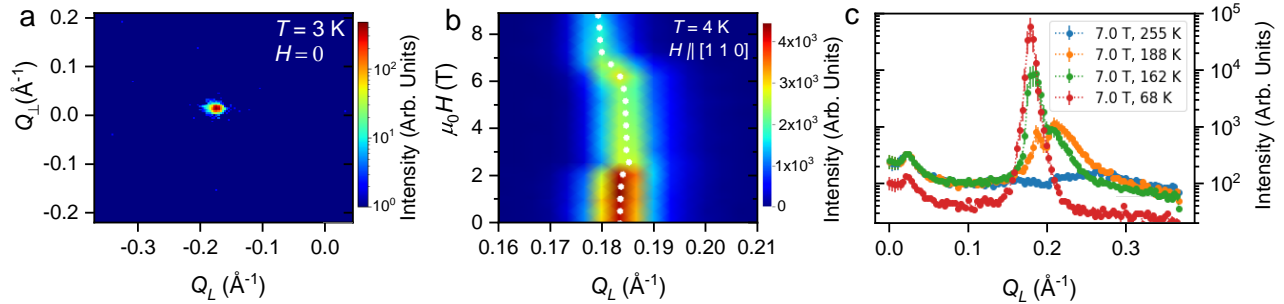
<sup>1</sup> Venturini, G., Idrissi, B. C. E. & Malaman, B. Magnetic properties of  $\text{RMn}_6\text{Sn}_6$  ( $\text{R} = \text{Sc}, \text{Y}, \text{Gd-Tm}, \text{Lu}$ ) compounds with  $\text{HfFe}_6\text{Sn}_6$  type structure. *Journal of Magnetism and Magnetic Materials* **94**, 35–42 (1991).

<sup>2</sup> Rosenfeld, E. V. & Mushnikov, N. V. Double-flat-spiral magnetic structures: Theory and application to the  $\text{RMn}_6\text{Sn}_6$  compounds. *Physica B* **403**, 1898–1906 (2008).

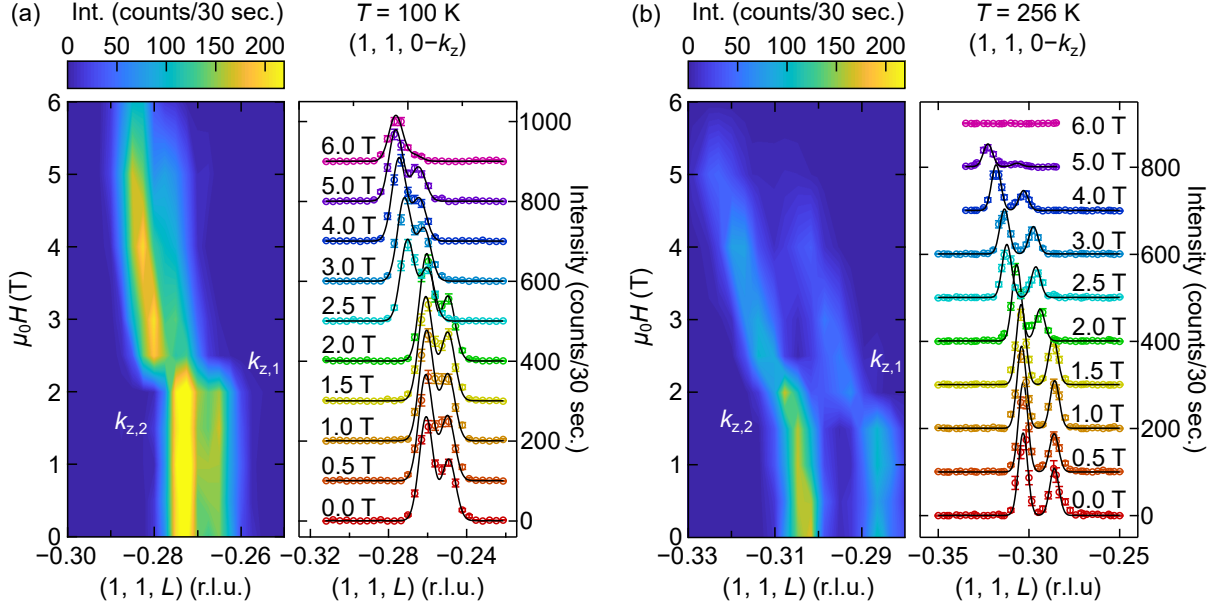
- <sup>3</sup> Rozenfel'd, E. V., Mushnikov, N. V. & Dyakin, V. V. Nested spirals in layered magnets. *Physics of Metals and Metallography* **107**, 557–568 (2009).
- <sup>4</sup> Nagaosa, N. & Tokura, Y. Topological properties and dynamics of magnetic skyrmions. *Nature Nanotechnology* **8**, 899–911 (2013).
- <sup>5</sup> Nagaosa, N., Sinova, J., Onoda, S., McDonald, A. H. & Ong, N. P. Anomalous Hall effect. *Reviews of Modern Physics* **82**, 1539–1592 (2010).
- <sup>6</sup> Nagaosa, N., Yu, X. Z. & Tokura, Y. Gauge fields in real and momentum spaces in magnets: monopoles and skyrmions. *Phil. Trans. R. Soc. A* **370**, 5806–5819 (2012).
- <sup>7</sup> Wang, W. *et al.* Spin chirality fluctuation in two-dimensional ferromagnets with perpendicular magnetic anisotropy. *Nature Materials* **18**, 1054–1059 (2019).

TABLE S1 : Calculated exchange and single-ion energies for the “Full”, “reduced”, and “minimal” models.

	Full model	Reduced Model	Minimal model
$J_1$	-12.86	-12.86	-12.86
$J_2$	7.26	4.66	4.66
$J_3$	-0.06	-2.20	-2.20
$J_4$	0.06	-	-
$J_5$	-0.16	-	-
$J_6$	0.54	-	-
$J_p$	-53	-53	-53
$K$	-0.31	-0.31	0.19
$J^z$	0.50	0.50	-



**FIG. S1 : Small angle neutron scattering (SANS) of  $\text{YMn}_6\text{Sn}_6$  .** (a) Background-subtracted SANS image on the two-dimensional position sensitive detector at 4 K and without a magnetic field applied. The data show a single incommensurate magnetic peak at a wave vector of  $Q = 0.184 \text{ \AA}^{-1}$ , corresponding to a real-space modulation of  $34 \text{ \AA}$  . No evidence for a skyrmion lattice was found at any temperature or field. (b) Intensity- $Q$  map of the field dependence of the Bragg peak at 4 K, revealing a series of phase transitions. The white dots are a guide to the peak center. (c) Cuts of the observed intensity through the magnetic peak at 7 T and for a series of temperatures, where it was discovered that at higher temperatures there are two closely-spaced incommensurate peaks. Subsequent wide-angle high resolution diffraction data revealed that there are two wave vectors at all temperatures. Note that the apparent peak at very small  $Q$  is simply due to an incomplete subtraction around the beam stop.



**FIG. S2 :** Temperature and magnetic field dependence of incommensurate magnetic Bragg peaks  $(1, 1, 0 - k_z)$ . a) The evolution of Bragg peaks  $k_{z,1}$  and  $k_{z,2}$  with an applied magnetic field at 100K and b) 256 K. For both (a) and (b), the solid black lines in the right-hand panels are Gaussian fits to the data as described in the text. An offset of 100 counts/30 sec. was added between individual  $L$  scans for clarity.

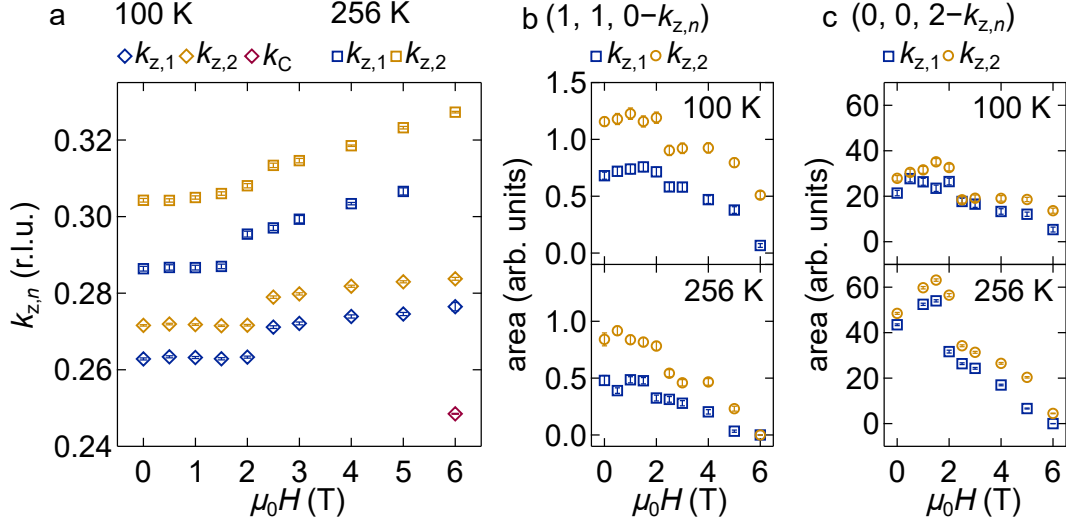


**FIG. S3 : Temperature and magnetic field dependence of wave vector and intensity of incommensurate magnetic Bragg peaks.** a) The evolution of wave vectors  $(0, 0, k_{z,1})$  and  $(0, 0, k_{z,2})$  depicted in Fig. 3(a) of the main text with applied magnetic field at 100 K and 256 K. An additional commensurate peak,  $k_c = 0.25$ , appears at 6 T in the 100 K data. b) Integrated intensity of the Bragg peaks  $(1, 1, 0 - k_{z,n})$  depicted in Fig. S2 at 100 K and 256 K. c) Integrated intensity of Bragg peaks  $(0, 0, 2 - k_{z,n})$  depicted in Figs. 3(b) and (c) of the main text as a function of magnetic field applied along  $[1, \bar{1}, 0]$ .



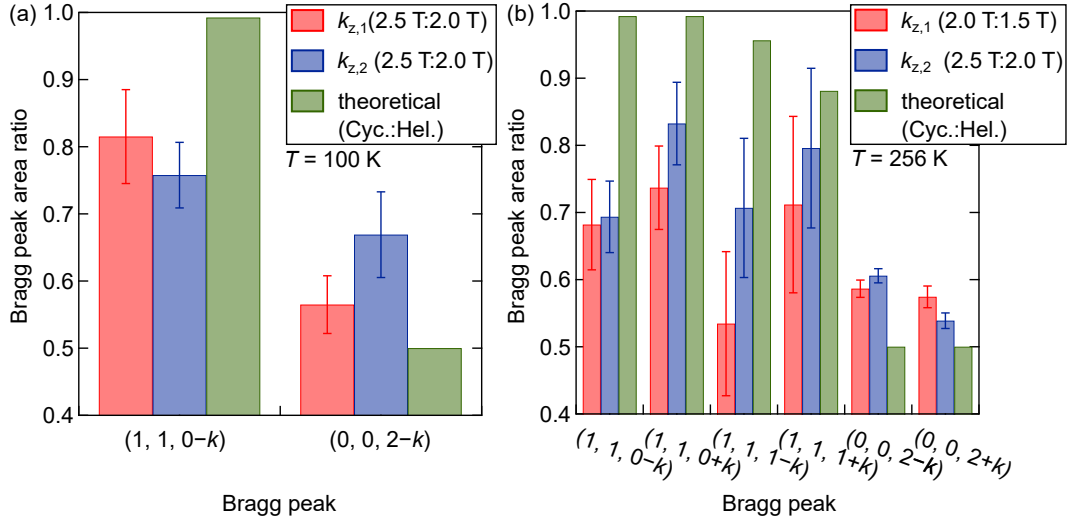


**FIG. S4 : Comparison of cycloidal vs helical spiral intensity.** Ratio of intensities just above  $H_1$  to just below  $H_1$  for the incommensurate Bragg peaks measured at (a) 100 K and (b) 256 K. The calculated values of the cycloidal:helical magnetic structure factor ratios are shown in green for comparison.

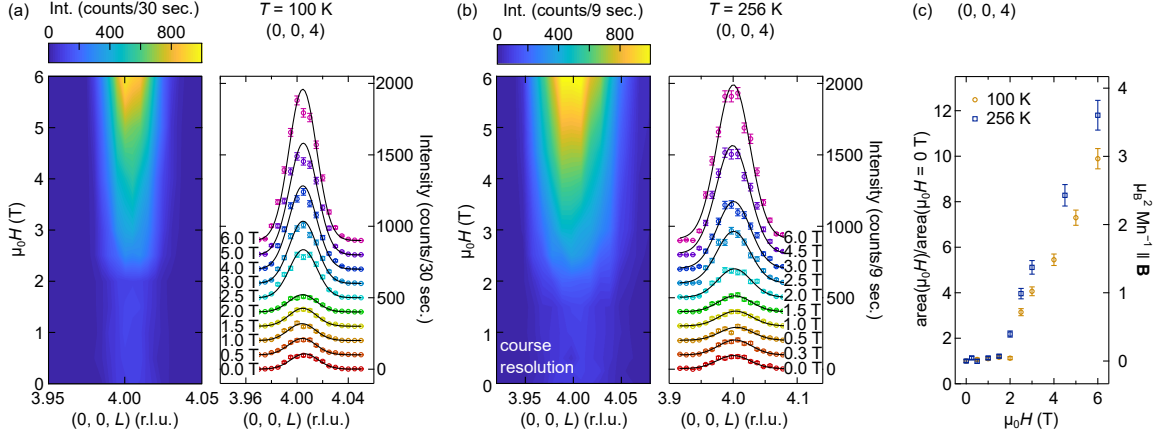


**FIG. S5 : Nuclear Bragg peak intensity as a function of magnetic field.**  $(0, 0, 4)$  Bragg peak intensity tracked at (a) 100 K and (b) 256 K as a function of applied magnetic field applied along  $[1, \bar{1}, 0]$  crystallographic axis. The increase in intensity as the field increases is indicative of a net component of magnetization emerging due to the moments canting towards the applied field direction. The solid lines in the righthand panels of (a) and (b) are the Gaussian fits to the data described in the text. An offset was added between individual  $L$  scans for clarity (offsets are 100 counts/30 sec. for (a) and 100 counts/9 sec. for (b)). Panel (c) shows the intensity versus  $H$ , divided by the intensity at  $H = 0$  where only the nuclear structure contributes intensity. The right hand axis displays the projection of the moment, in  $\mu_B^2 \text{Mn}^{-1}$ , along the applied field direction.

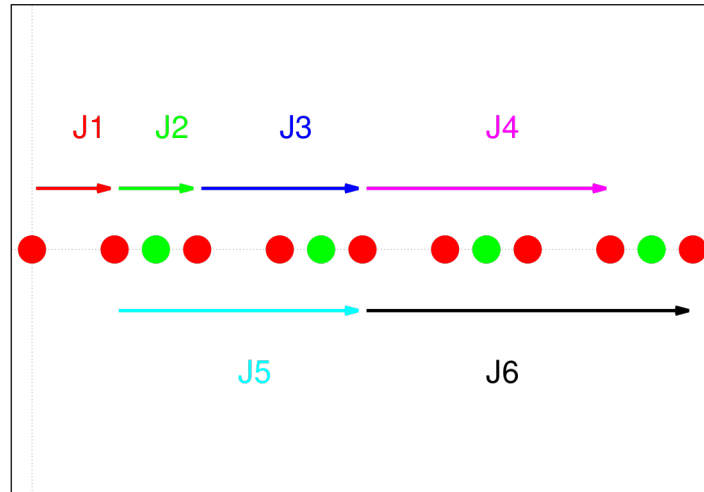


**FIG. S6 : Schematic of exchange interactions along  $c$ -axis.** First 6 exchange interactions between Mn layers. Red: Mn layer; green: spacer layer including Y [see Fig. 1(a) of the main text]

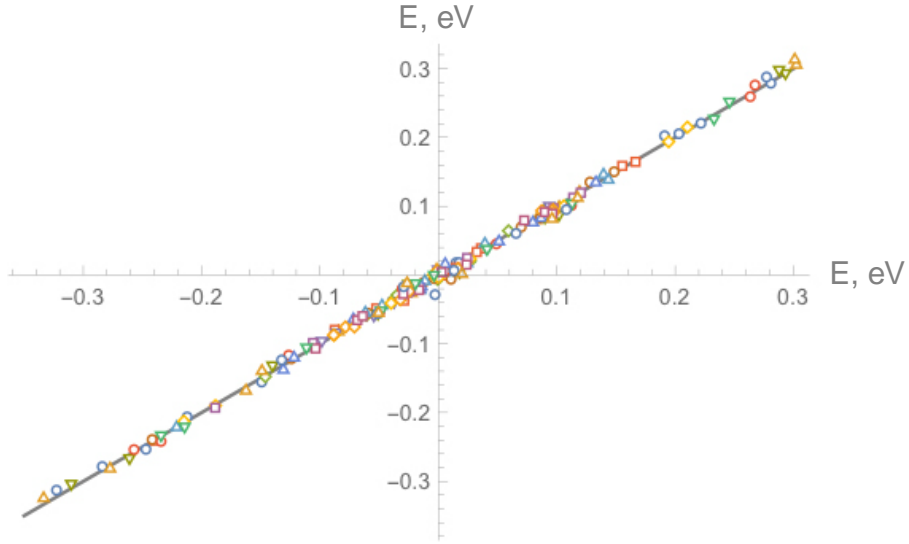


**FIG. S7 :** Fitted vs. calculated values of total energies (deviations from the straight line indicate fitting errors). Blue circles are the calculated values for  $U - J = 0$ . Other symbols are for other values of  $U$ .

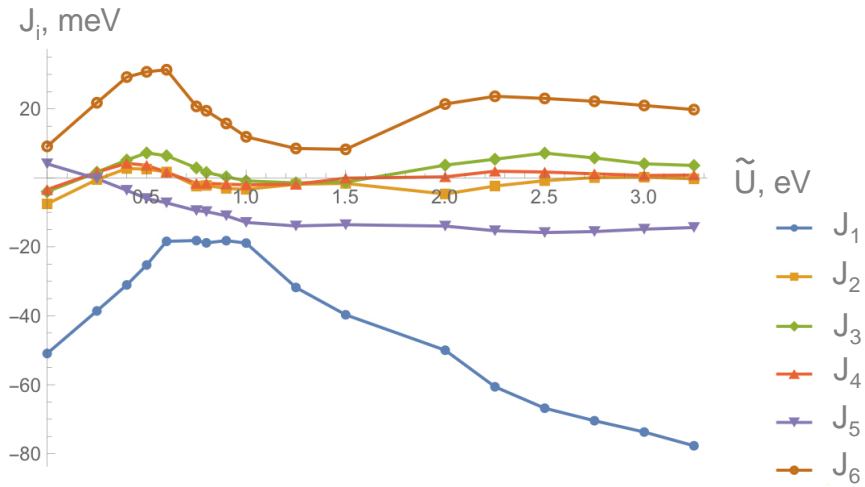


**FIG. S8 :** Fitted values of the exchange constants  $J_1$ - $J_6$  as a function of  $\tilde{U} = U - J$ .

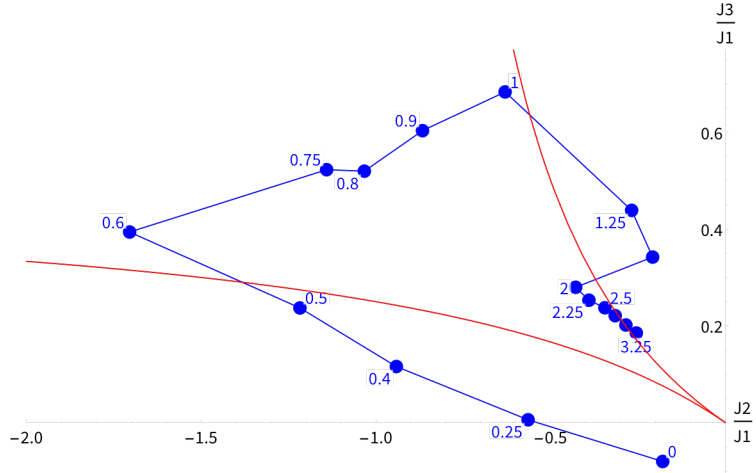


**FIG. S9 :** Phase diagram of the  $J_1 - J_2 - J_3$  model in the  $J_2/J_1 - J_3/J_1$  coordinates. The region between the two red lines is a spiral state, above them is the FM, and below the AF *uudd* state. The points reflect the calculated values of  $J_1, J_2, J_3$  for different values of  $U - J$ .

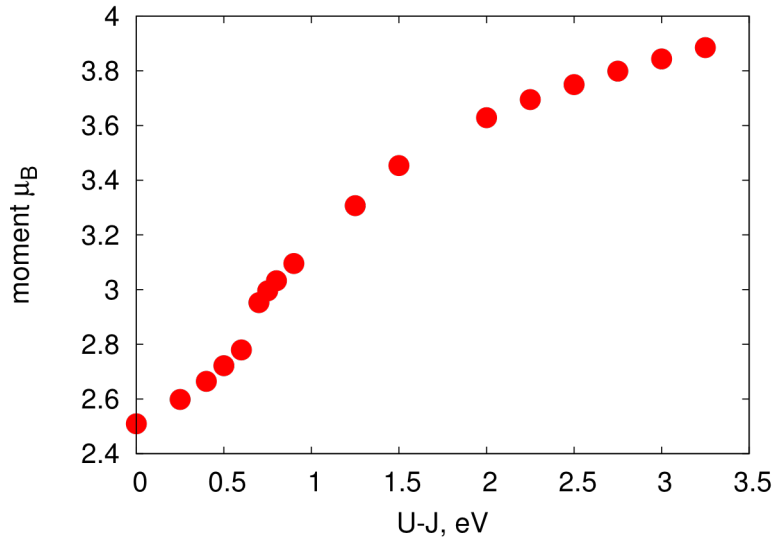


**FIG. S10 :** Calculated magnetic moments on Mn (square-averaged over all 8 sites and all 10 configurations) as a function of  $U - J$ .

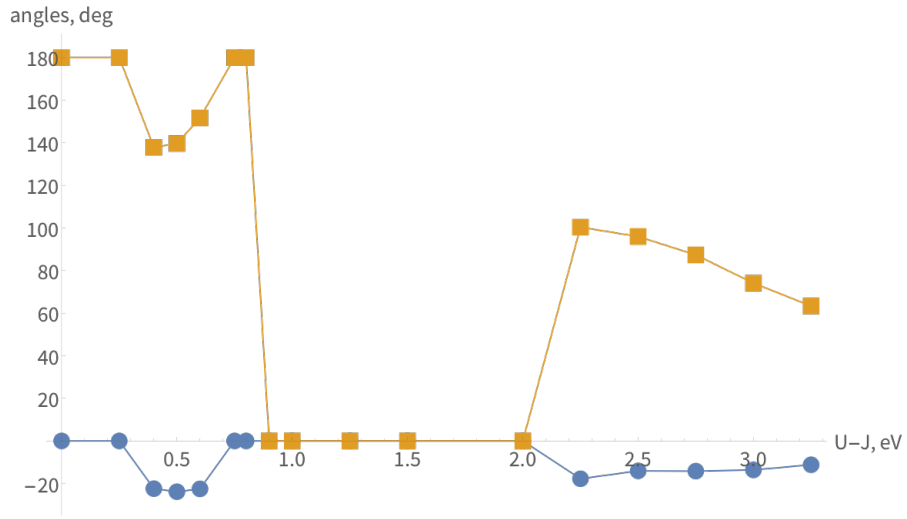


**FIG. S11** : Calculated spiral angles  $\alpha$  and  $\beta$  (see the text for the definitions).

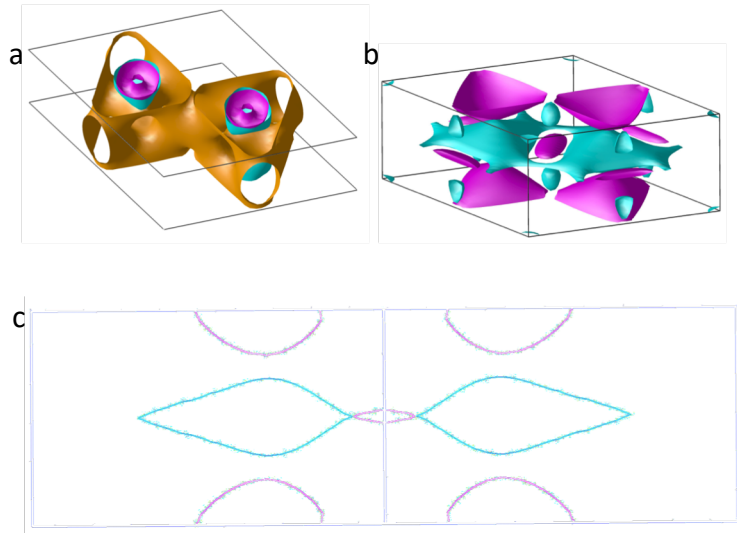


**FIG. S12** : Calculate Fermi surface (no Hubbard  $U$ ) for the ferromagnetic ordering, for a) the spin-minority and b) spin-majority electrons. c) A vertical cut of the spin-majority Fermi surface in the  $\Gamma$ -K-K-A plane.

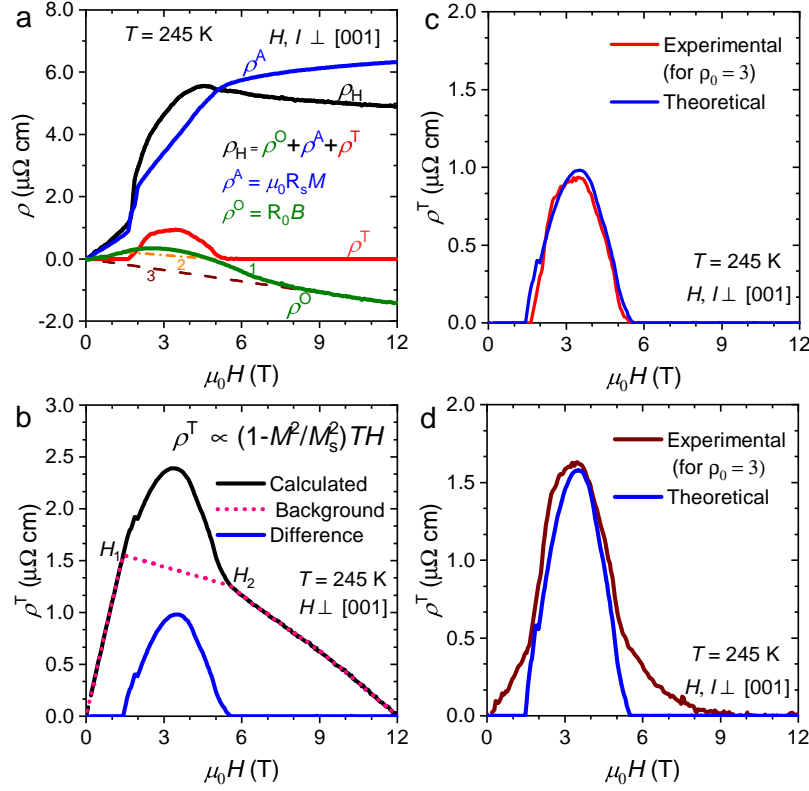


**FIG. S13 :** Estimation of topological Hall resistivity at 245 K from measured data and theoretical model. a) Hall resistivity and its various components. Three different  $\rho^0$  are labelled as 1, 2 and 3 and are discussed in the text in SI5. b) Topological Hall effect calculated using the chiral spin texture model discussed in SI4. Since there is no THE outside of TCS phase, the component obtained outside this phase is subtracted as a background (pink dashed line) from the calculation carried out in the entire field range (black solid line) from 0 to 12 T to obtain the THE (blue solid line) in the TCS phase. c) Topological Hall resistivity estimated using  $\rho^0$  labelled as 1 in panel (a) compared to that obtained from the theoretical model. d) Topological Hall resistivity estimated using  $\rho^0$  labelled as 3 in panel (a) compared to that obtained from the theoretical model. Results presented in panels (c) and (d) show that the theoretical model describes the experimental data well irrespective of the method used to estimate the ordinary component of the Hall resistivity ( $\rho^0$ ).

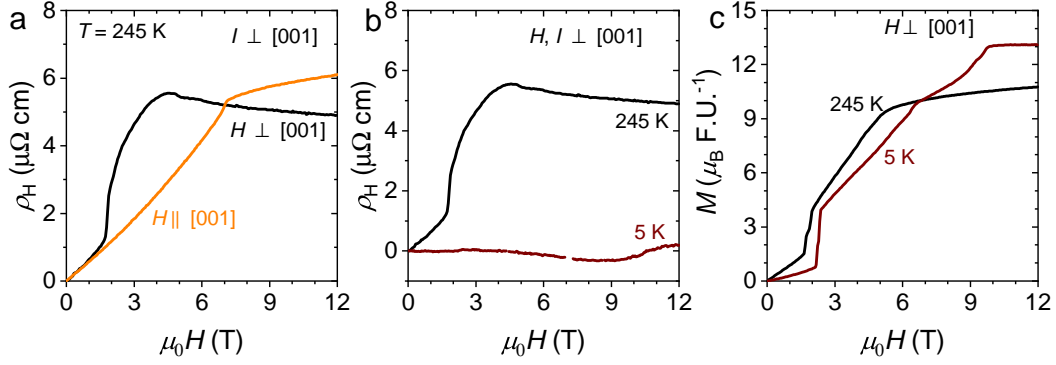


**FIG. S14 :** Hall resistivity and magnetization of  $\text{YMn}_6\text{Sn}_6$ . a) Hall resistivity at 245 K measured with magnetic field in the  $ab$ -plane and along the  $c$ -axis. The current was applied along the same direction in these two measurements carried out on two different samples. b) Hall resistivity at 5 K and 245 K measured with magnetic field applied in the  $ab$ -plane. c) Magnetization at 5 K and 245 K measured with the magnetic field in the  $ab$ -plane.

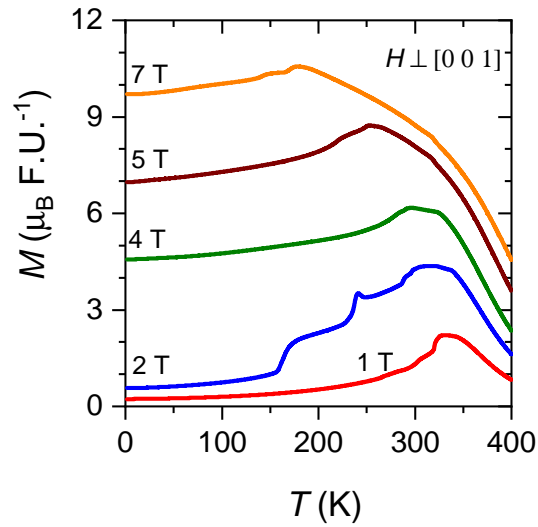


**FIG. S15 :** Magnetic moment of  $\text{YMn}_6\text{Sn}_6$  as a function of temperature. Magnetic moment as a function of temperature at indicated magnetic fields applied in the  $ab$ -plane. Above 3 T and below 250 K, magnetic moment changes very little with the temperature.